Renewable Energy 225 (2024) 120344

Contents lists available at ScienceDirect

Renewable Energy

journal homepage: www.elsevier.com/locate/renene

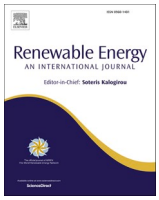

Array analysis on a seawall type of deformable wave energy converters

Yujia Wei [a,1], Chao Wang [b,1], Wenchuang Chen [c,**], Luofeng Huang [a,*]

[a] School of Water, Energy and Environment, Cranfield University, Cranfield, MK43 0AL, UK
[b] State Key Laboratory of Coastal and Offshore Engineering, Dalian University of Technology, Dalian, 116024, China
[c] School of Civil Engineering, Sun Yat-Sen University, Zhuhai, 519082, China

ARTICLE INFO

Keywords:
Wave farm
Flexible wave energy converter
Hydroelasticity
Fluid-structure interaction
Computational fluid dynamics
Multiple deformable structures in waves

ABSTRACT

There has been a significant interest in developing Flexible Wave Energy Converters (FlexWECs) that utilise structural deformations to generate electricity and mitigate destructive wave loads to the devices. In the meantime, FlexWECs are most likely to operate in an array format to enhance space usage and power output, as well as provide convenience for maintenance. In this context, the present paper develops a high-fidelity computational model to investigate the interaction of ocean surface waves with an array of seawall-type FlexWECs, which can meanwhile serve coastal engineering purposes. The fluid field is solved using the Navier-Stokes equations, and structural deformations are predicted using a nonlinear finite-element method. Hydroelastic interactions of up to seven deforming FlexWECs with the surrounding wave fields are demonstrated through systematic simulation cases. Based on the simulation results, analyses are conducted to investigate how the wave farm energy output is influenced by the gap between individual devices and the number of devices deployed. Accordingly, empirical design suggestions are provided. Overall, this work innovatively simulates the hydroelastic interactions between waves and multiple deforming structures, and the provided insights are useful for promoting the development of FlexWECs and their wave farms.

1. Introduction

The concept of Wave Energy Converter (WEC) can be traced back to 1799 [1], and by the late 20th century, several hundred patents related to WEC had existed [2,3]. However, the current advancement of WECs has yet to fulfil the prerequisites for large-scale commercial expansion. A common challenge is to deploy large devices in the inherently energetic ocean environment, posing risks in operations [4,5]. The recent innovation in Flexible-body WECs (FlexWECs) has become a promising direction to complement conventional rigid-body designs [6–12]. The flexibility can effectively mitigate wave loads thus addressing the survivability issue [13], whilst the wave-induced deformation of the whole structure can be utilised to generate electricity [7,14].

FlexWECs are typically deformable structures in waves, combined with a Power Take-Off system (PTO) that utilises the Dielectric Elastomer Generators (DEG) technology. The working principle of such a DEG system has been reviewed by Collins et al. [7] and Moretti et al. [15]. To briefly summarise, the surface of the WEC structure can be made of soft membranes that can accommodate geometrical deformations. The DEGs can contain layers of conductive electrodes, and it generates electricity when the electrodes are moved. When a flexible structure is constantly changing its shape due to oscillating wave loads, it provides a power output [16,17].

A trending investigation of DEG FlexWECs has been conducted jointly by the universities of Trento, Plymouth and Edinburgh, named the PolyWEC project [18] and the ELASTO project [19]. The projects demonstrated the feasibility and laid the groundwork for the future development of this type of devices. Similar projects, such as the WETFEET project [20] and the WES-PTO program [21], also supported the development and testing of various FlexWECs in the field. Another innovative project DEEC-TECS, from the National Renewable Energy Laboratory (NREL), presented a few prototype designs for the potentially applicable FlexWECs [22]. To date, over 20 pioneering FlexWECs have been devised, many of which have been built and sea trialed, e.g., the Anaconda WEC [23], SBM S3 [16] and AWS Electric Eel [24]. These deformable WEC designs have offered a possible route to overcoming

* Corresponding author.
** Corresponding author.
E-mail addresses: yujia.wei@cranfield.ac.uk (Y. Wei), 201352094@mail.dlut.edu.cn (C. Wang), chenwch37@mail.sysu.edu.cn (W. Chen), luofeng.huang@cranfield.ac.uk (L. Huang).
[1] These authors have contributed equally and share the first authorship.

https://doi.org/10.1016/j.renene.2024.120344
Received 10 August 2023; Received in revised form 29 January 2024; Accepted 15 March 2024
Available online 19 March 2024

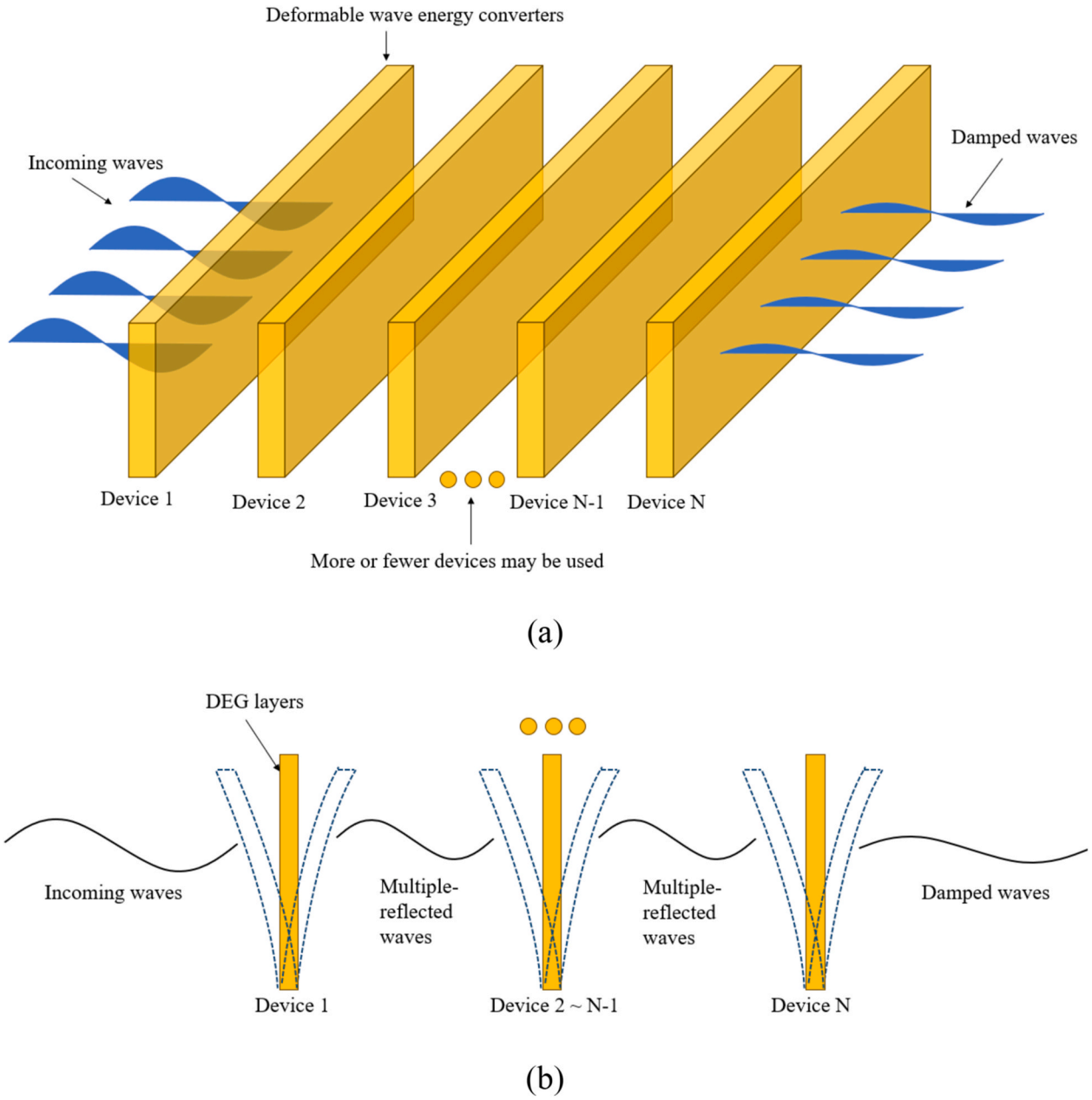

Fig. 1. Schematic of the wave farm consisting of multiple seawall-type deformable WECs, inspired by NREL [22]. (a) General arrangement, (b) Profile view to illustrate the working mechanism.

WEC's structural issues, showing the potentail for upscaling and market development [7]. This has created a FlexWEC branch that is considered one of the biggest ever in the WEC sector, providing significant commercial and funding opportunities [25]. Accordingly, there has been a significant research interest, in which appropriate modelling of the FlexWECs is essential.

The modelling procedures for FlexWECs require consideration of complex multi-physics. This involves structural deformations in waves that are based on coupled Fluid-Structure Interactions (FSI), i.e., any deformation of the structure triggers a response of the wave flow and vice versa. In the FlexWEC field, such modelling is still lacking [7]. A potential way to realise this is using the partitioned approach [26], and there have been examples ranging from reduced-order models [27,28], steady-state models [29,30], and high-fidelity simulations [31–38].

Although previous research has been valuable for the design and modelling of a single FlexWEC device operating in isolation [33], there have been limited attempts to investigate a wave farm with multiple FlexWECs. Wave farm consisting of multiple identical devices is essential for the deployment of WEC devices in terms of best utilising ocean space, enhancing power generation and providing convenience to operation and maintenance. However, in the wave farm case, FlexWECs are placed in close proximity and the interaction of waves with one device can influence other devices. Thus, results from previous research that studying a FlexWEC operating in isolation cannot be directly scaled for evaluating a wave farm containing more devices.

Quantities of interest for wave farms include the reflection, transmission and scattering of waves passing through a WEC array [39,40] as well as the performance of every individual WEC [41]. Zheng et al. [38] analysed the hydroelastic interaction between water waves and circular floating elastic plates array using a theoretical model based on linear potential flow theory and an eigenfunction matching method [42]. An interesting phenomenon was observed that, when structures were placed in regular patterns separated by a distance equal to half the wavelength of the incoming wave, focussed waves were captured,

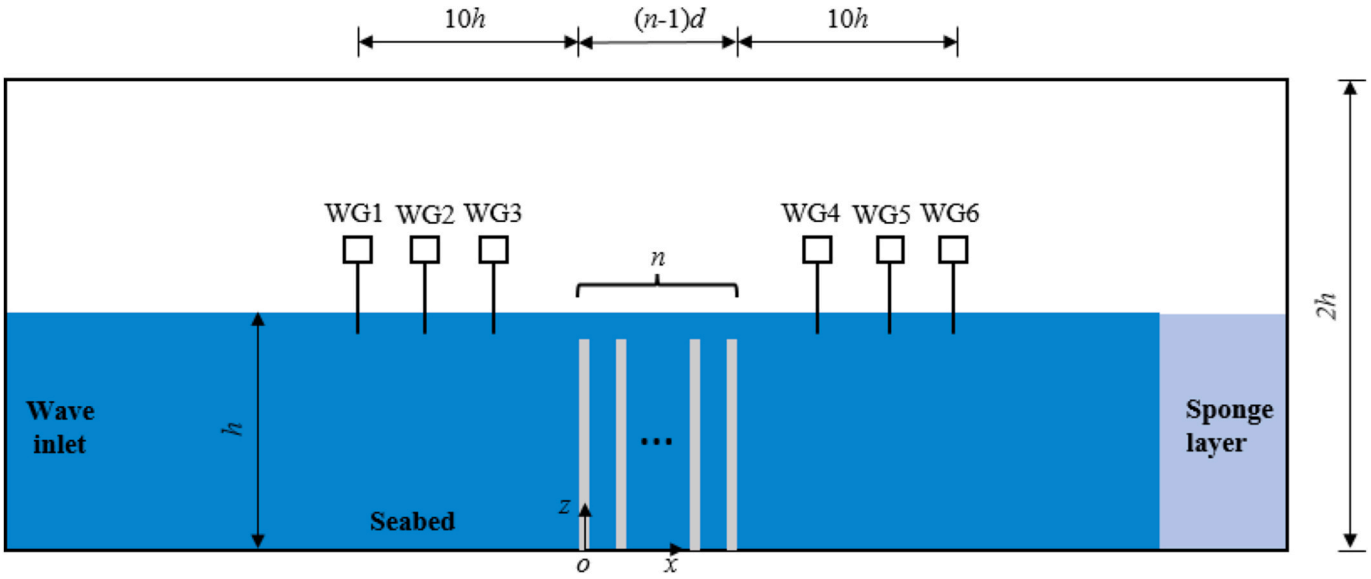

Fig. 2. Schematic diagram of the computational model.

similar to the Bragg resonance [43]. It was suggested that this resonance happens when incident waves are twice as long as the spacing [43]. However, it is unclear whether these phenomena exist in FlexWEC arrays. Nové-Josserand et al. [43] presented an interference model to predict optimal configurations of multiple flexible blades in monochromatic waves, and they investigated various parameters including the number of blades, their spacing, and their flexibility. The authors found that the wave transmission coefficient is greatly affected by the number of rows, and the results showed that the wave transmission would reduce to approximately 8% when the row number reaches 7 for all array spacing [38].

On the other hand, there has been a recent shift of research interest from sole WECs to multiple-purpose structures of WECs as coastal defence [44]. Typical examples can be seen as integrated Oscillating-Water-Column WECs in seawalls [45]. Since traditional seawalls were designed to dissipate waves, the integration of WECs harnesses this part of dissipated power instead, making the coastal structures also equip renewable energy purposes. In terms of FlexWECs, this is viable through a vertical-wall type of deformable WEC originally proposed by NREL [22]. The concept of applying this FlexWEC as a wave farm as well as a coastal managing structure is illustrated in Fig. 1. When incident waves approach a flexible wall WEC, it induces the WEC to deform forward and backwards, whilst the upstream WEC acts as a wave generator and transfers power to downstream WECs. There will be multiple reflections of waves between the deforming structures, which make the problem complex to analyse. The optimal amount of WECs to be deployed and the gap between the WECs need to be investigated.

In this context, the present work develops a fully nonlinear computational FSI model for simulating the interaction between waves and an array of seawall-type FlexWECs, which is based on coupling Computational Fluid Dynamics (CFD) and Computational Solid Mechanics (CSM). The study presents simulations involving up to seven FlexWECs operating in a row, showing the energy performance of each device as well as the overall array under a range of regular waves. Extensive analyses are given on the optimal separation distances between devices as well as the optimal number of devices deployed. Novel design suggestions are given accordingly. This is novel that a CFD + CSM approach has been realised for simulating multiple deformable structures in waves [37], which is a step forward from the recent states of art that simulated a single deformable structure in waves [33].

This paper is organised as follows: Section 2 describes the problem definition and the corresponding FSI approach to simulate this. Section 3 presents the verification procedure. Section 4 elaborates on the simulation results, discussing the effects of separation distance between FlexWECs and the number of FlexWECs deployed; this starts with two devices operating in a row and gradually extends to seven devices. Finally, concluding remarks are drawn in Section 5.

2. Computational approach

Inside the FSI framework, the fluid and solid domains are typically discretised into two independent meshes. The fluid field is solved by CFD, and the deforming WECs are modelled by CSM. Meanwhile, the CFD and CSM parts are stitched together through an FSI algorithm. All code applied in this work was programmed by the authors.

2.1. Computational domain and boundary conditions

In this study, a computational domain is established in two dimensions, i.e., $-10L < x < 10L$, $0 < z < 2h$, where L and h refer to the incident wavelength and water depth, respectively. A Cartesian coordinate system is applied, with x-axis pointing toward the wave propagation direction and z-axis toward the vertical direction. Within the computational domain, a series of wave gauges represented (WG1–WG6) are placed to monitor the wave elevations in the time domain. WG1 is arranged at a distance of $-10h$ before the first WEC, and the distances between WG1–WG2 and WG2–WG3 are $0.2L$ and $0.3L$, respectively. The reflected wave generated by the FlexWECs is evaluated using the wave reflection analysis method proposed by Ref. [46], based on the wave elevation data recorded by wave gauges WG1–WG3. WG6 is $10h$ away from the last beam, and WG4 and WG5 are $0.5L$ and $0.2L$ away from WG6 respectively. Fig. 2 illustrates a generic case of placing N FlexWECs. The FlexWECs are placed at the wave propagation region, separated by a distance of d and fixed to the seabed at their bottoms.

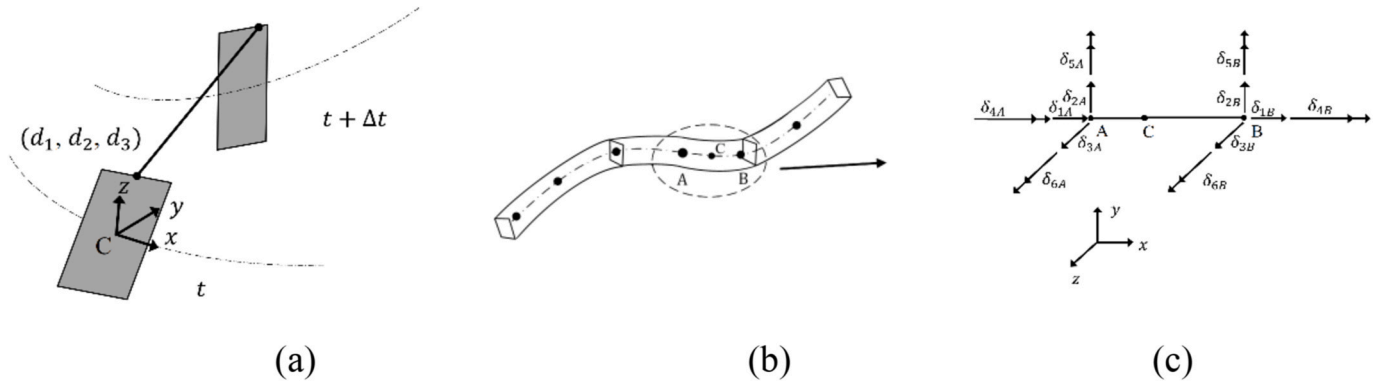

Fig. 3. Illustration of the structural model (a) The displacement of a point on the cross-section from t to $t + \Delta t$ with the central axis in the x direction; (b) Schematic diagram of a discretised slender body, the elliptical dashed line highlights one beam element with two nodes (A, B); (c) A beam element with 12 degrees of freedom.

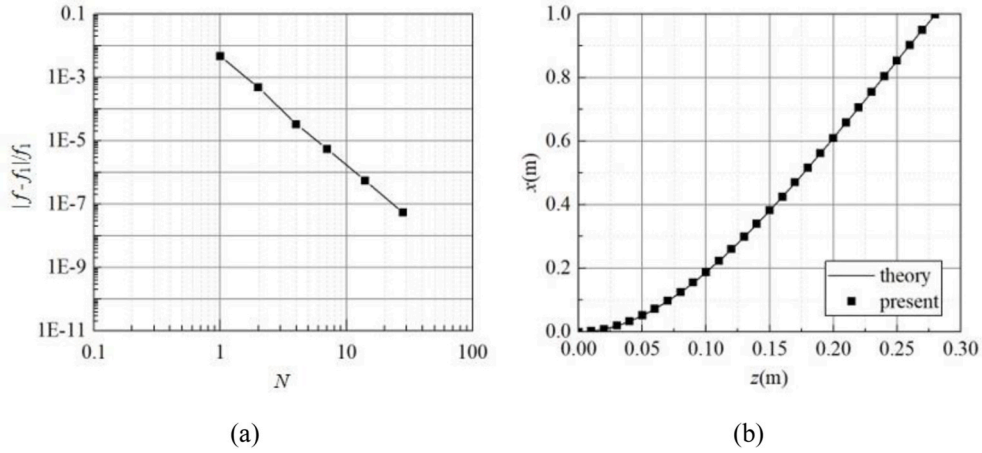

Fig. 4. Uncertainty analysis of the structural model. (a) Relative error of the first natural frequency under different elements; (b) First mode of the structure with 28 elements.

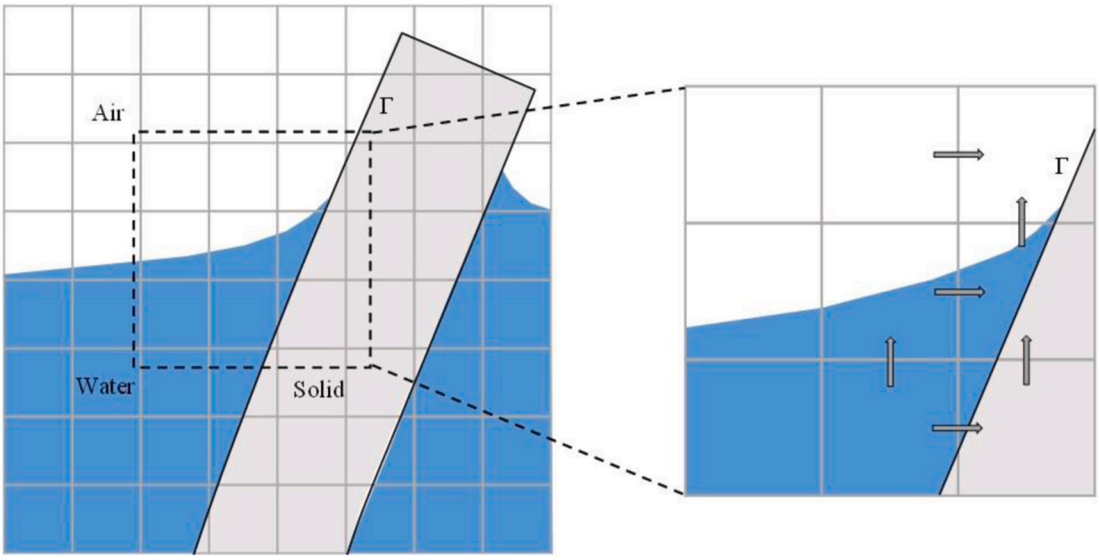

Fig. 5. Close-up view of the discretisation and information change at the fluid-structure interface.

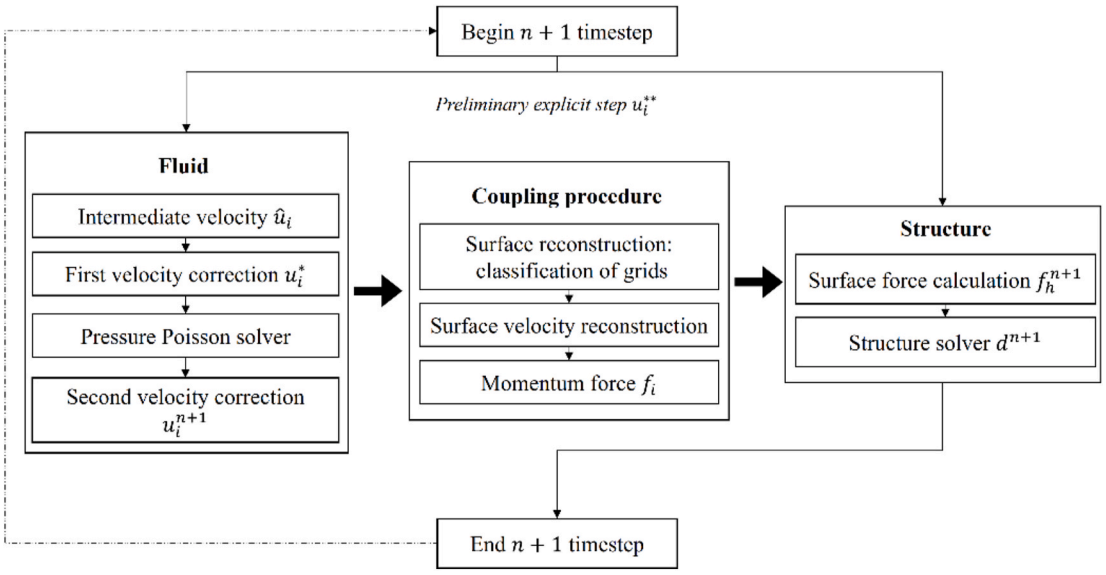

Fig. 6. Illustration of the FSI workflow.

Table 1
Structural and wave properties in the model of a single deforming seawall.

Parameters	Value
Wave height, H	0.04 m
Wave frequency, f_w	1 Hz
Water depth, h	0.3 m
WEC height, h_s	0.35 m
WEC width, b	0.02 m
Mass coefficient, $\gamma = \rho_s\, b/\, \rho_w\, h$	0.08
Stiffness coefficient, $\beta = EI/\, \rho_w gh^4$	0.10, 0.15, 0.20, 0.25, 0.30, 0.40, 0.60, 1.00, 5.00

The boundary conditions are set as follows. In the fluid sub-domain, the left and right-sides boundaries are specified as wave inlet and wave outlet, respectively. The wave inlet is set to generate regular incident waves, and a dissipative zone with a length of $2L$ is placed at the right end of the computational domain to absorb the wave. The bottom and the top boundaries are set as no-slip wall and static-pressure conditions, respectively. In the solid sub-domain, the bottoms of the FlexWECs are set as fixed boundary conditions, and the remaining boundaries of the FlexWECs are allowed to freely deform.

2.2. CFD solver

In this study, CFD is used to obtain fluid solutions by solving the Navier-Stokes equations, i.e., the velocity and pressure fields, and the Volume-of-Fluid (VOF) method is used to track the interface of air and water. The Navier-Stokes equations for incompressible flow can be written as follows:

$$\nabla \cdot \mathbf{u} = 0 \tag{1}$$

$$\frac{\partial(\rho \mathbf{u})}{\partial t} + \nabla \cdot (\rho \mathbf{u}\mathbf{u}) = -\nabla p + \nabla \cdot \left(\mu\left(\nabla \mathbf{u} + \nabla \mathbf{u}^T\right)\right) + \rho \mathbf{g} + \mathbf{f} \tag{2}$$

where t is time, $\mathbf{u} = \{u, w\}$ is the velocity vector, ρ denotes the fluid density, and p is the pressure. $\mathbf{g}$ is the gravitational acceleration. $\mathbf{f}$ denotes the sum of other external forces, i.e. the reacting force from FlexWECs in this study. The VOF method sets a scalar α, as the scalar function with a value of 1 in the fluid phase, 0 in the gas phase and a value between 1 and 0 indicates the free surface. Then the density and dynamic viscosity μ in the two-phase flow can be expressed as:

$$\rho = \rho_w \alpha + \rho_a (1-\alpha), \mu = \mu_w \alpha + \mu_a (1-\alpha) \tag{3}$$

Table 2
Three tested mesh densities in the refined region.

Mesh grid	Coarse	Medium	Fine
Δx	$b/2$	$b/4$	$b/8$
Δz	$h_s/\,50$	$h_s/\,100$	$h_s/\,200$
Cell number	137,600	222,600	639,600

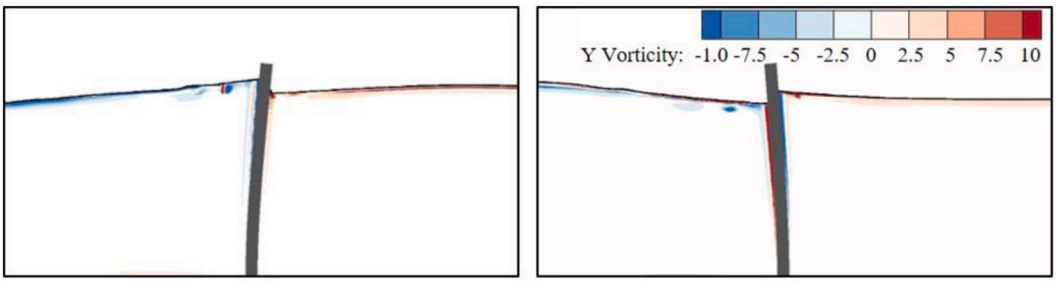

Fig. 7. Verification case example against [33]. (a) $D_x = D_{x,max}$ and (b) $D_x = D_{x,min}$.

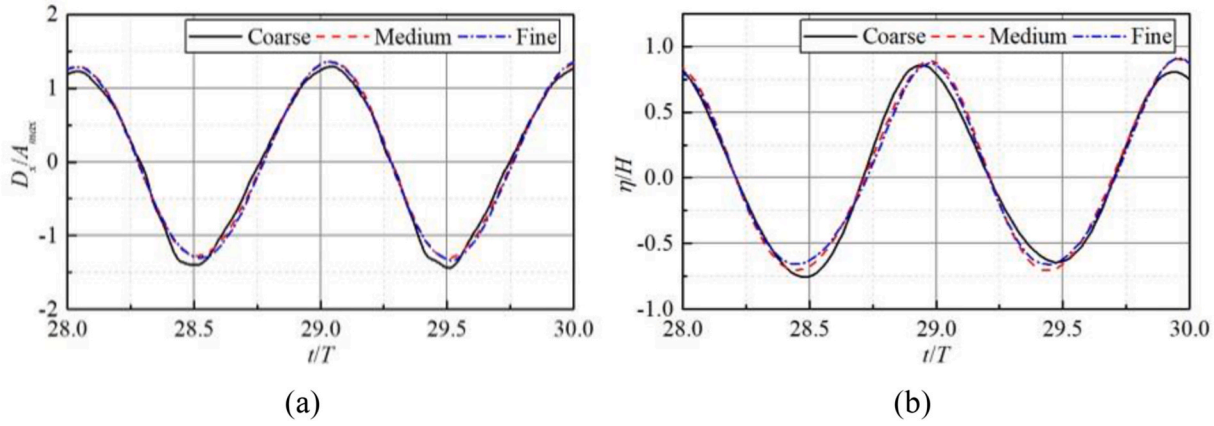

Fig. 8. Comparison of coarse, medium and fine grids. (a) Time series of horizontal displacement, (b) Time series of wave elevation.

Table 3
Grid convergence analysis with three mesh densities ($\beta = 0.1$).

	Coarse	Medium	Fine	Hu et al. [33]
Maximum deflection $D_{x,max}/A_{max}$	1.315 (−6.724%)	1.378 (−2.277%)	1.389 (−1.454%)	1.410
Reflection coefficient k_r	0.546 (+10.66%)	0.521 (+5.532%)	0.527 (+6.748%)	0.494

Table 4
Time convergence test studies with three time steps ($\beta = 0.1$).

Time step size	1/625T	1/1250T	1/2500T	Hu et al. [33]
Maximum displacement $D_{x,max}/A_{max}$	1.347 (−6.775%)	1.378 (−2.277%)	1.404 (−0.433%)	1.410
Reflection coefficient k_r	0.529 (+7.133%)	0.521 (+5.532%)	0.525 (+6.424%)	0.494

where ρ_w denotes the density of water, ρ_a denotes the density of air, μ_w denotes the dynamic viscosity of water, and μ_a represents the dynamic viscosity of air. The transport equation for C can be derived from the continuity equation:

$$\frac{\partial \alpha}{\partial t} + \nabla \cdot (\alpha \mathbf{u}) = 0 \tag{4}$$

A fractional step method [47] with a second-order overall accuracy is applied to decouple velocity and pressure. The momentum equation is discretised in time semi-implicitly. The convection and diffusion terms in the momentum equation are discretised by the second-order Adams–Bashforth scheme and Crank–Nicolson scheme respectively. The advection of α and the four step projection methods are described as follows:

Table 5
Structural and wave properties in the present simulations.

Structure and fluid parameters	Value
Wave Height, H_s	0.03 m
Wave period, T	1.0 s
Wave length, L	1.37 m
Water depth h	0.3 m
Beam length, h_s	0.28 m
Beam thickness, b	0.02 m
Solid density, ρ_s	1200 kg/m^3
Young modulus, E	3.0 MPa, 6.0 MPa, 12 MPa, 24 MPa, 100 MPa
Number of rows, N	2, 3, 5, 7
Separating distance, d/L	0.2, 0.25, 0.4, 0.5, 0.6, 0.8, 1.0, 1.4, 1.5, 1.8

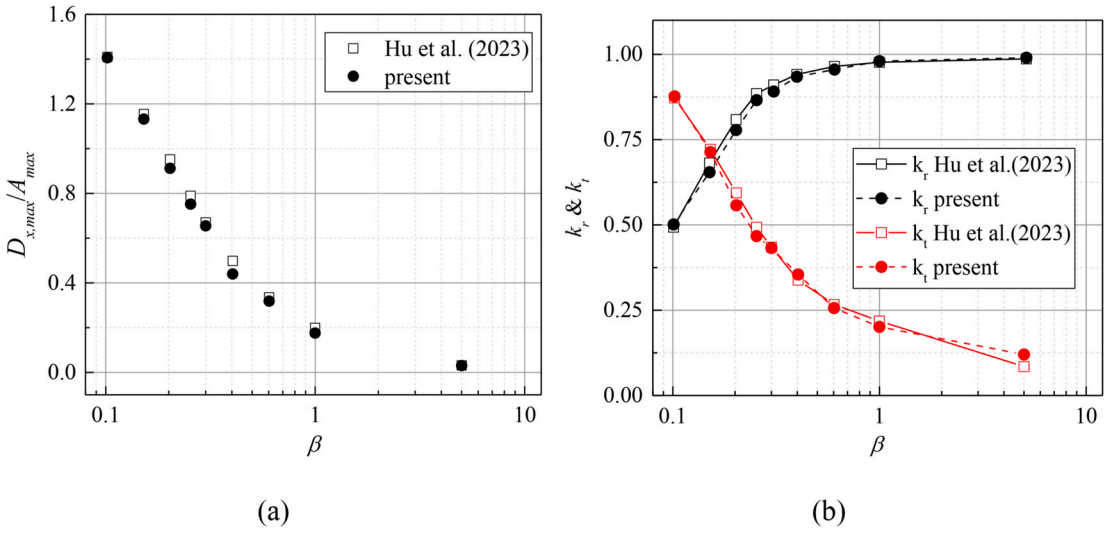

Fig. 9. Comparison of the present model with experimental results [33]. (a) Beam deflection at the free end, (b) Wave reflection and transmission for different structural stiffnesses β.

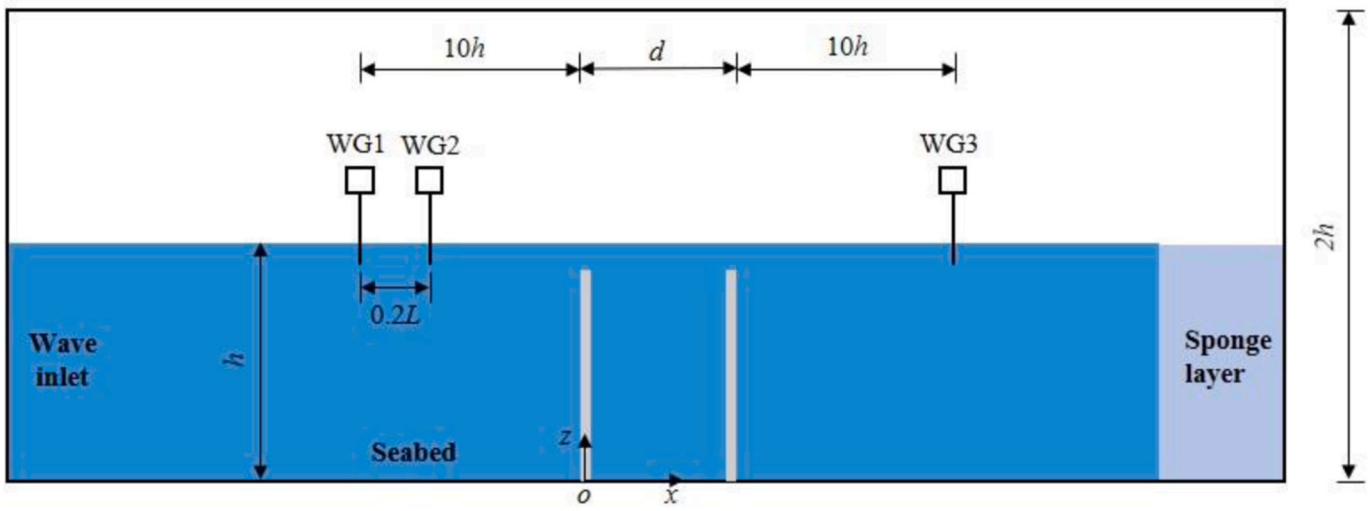

Fig. 10. Dual FlexWECs in the wave tank.

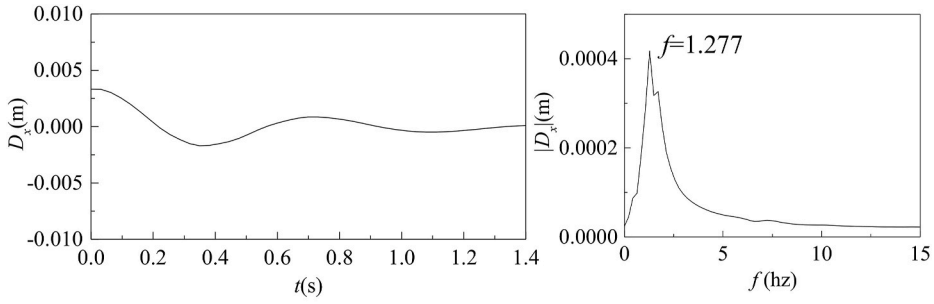

(a) E = 3 MPa

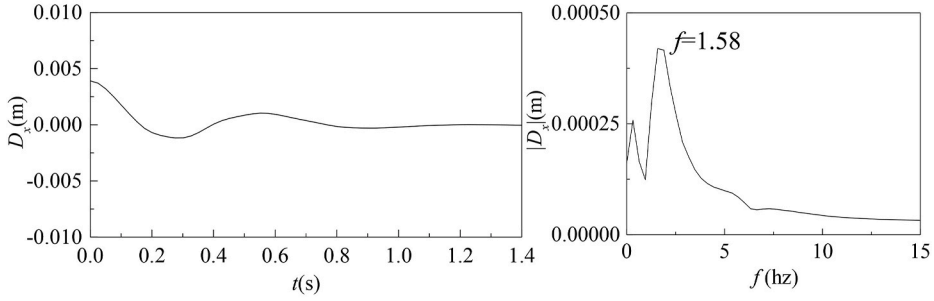

(b) E = 6 MPa

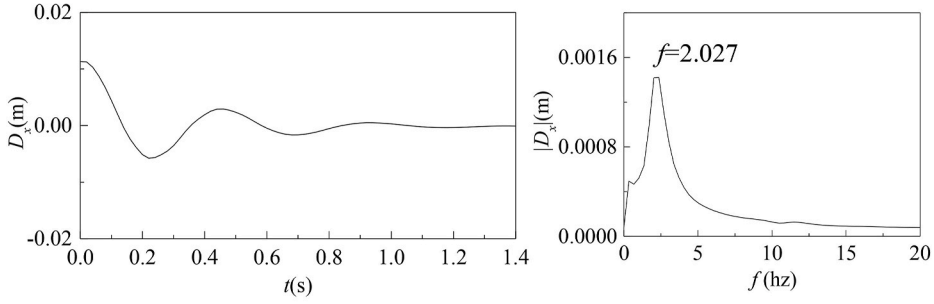

(c) E = 12 MPa

Fig. 11. Time and frequency analysis of the beam's wet natural frequency at different Young's modulus.

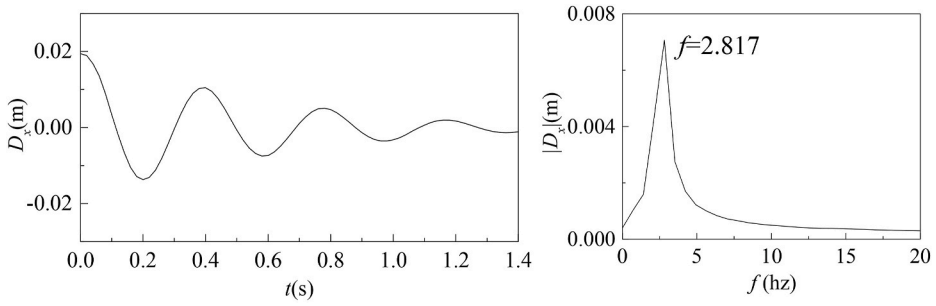

(d) E = 24 MPa

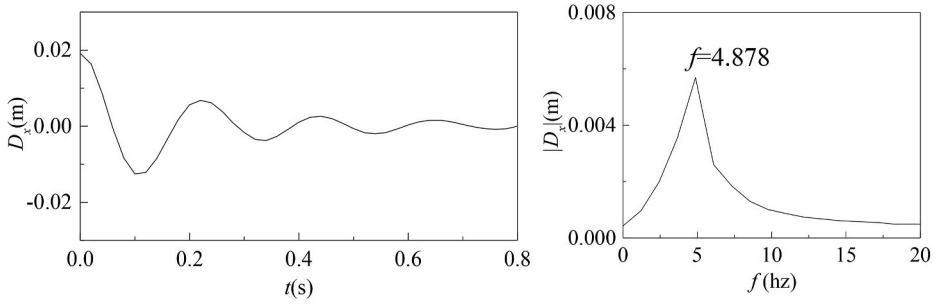

(e) E = 100 MPa

Fig. 11. (*continued*).

$$\alpha^{n+1} = \alpha^n - \Delta t L_{vof}(\mathbf{u}^n), \tag{5}$$

$$\rho^{n+1}\hat{\mathbf{u}} = \rho^n \mathbf{u}^n + \Delta t\left[-\frac{3}{2}L_{conv}(\alpha^n, \mathbf{u}^n) + \frac{1}{2}L_{conv}(\alpha^{n-1}, \mathbf{u}^{n-1}) + \frac{1}{2}L_{diff}(\alpha^n, \mathbf{u}^n) + \frac{1}{2}L_{diff}(\alpha^{n+1}, \hat{\mathbf{u}}) + \mathbf{f}^{n+1}\right] \tag{6}$$

$$\frac{\mathbf{u}^* - \hat{\mathbf{u}}}{\Delta t} = \frac{1}{\rho^{n+1}}\nabla p^n \tag{7}$$

$$\nabla \cdot \left(\frac{1}{\rho^{n+1}}\nabla p^{n+1}\right) = \frac{1}{\Delta t}\nabla \cdot \mathbf{u}^* + \nabla \cdot \mathbf{g} \tag{8}$$

$$\mathbf{u}^{n+1} = \mathbf{u}^* - \frac{\Delta t}{\rho^{n+1}}\nabla p^{n+1} + \mathbf{g} \tag{9}$$

where $\hat{\mathbf{u}}$ and $\mathbf{u}^*$ are the first and second intermediate velocities, respectively, L_{conv} and L_{diff} represent the spatial operators for the convective and diffusion terms of momentum, respectively, and the superscript n denotes the n-th time step. For spatial discretisation of terms in Equation (6), the convection terms are discretised using a third-order Quadratic upwind (QUICK) scheme [48] and the diffusion terms are discretised using a second-order central difference scheme.

The incident wave is generated based on the second-order Stokes wave theory, with the resulting expression of free surface and velocity components are:

$$\eta = \frac{H}{2}\left[-\frac{Hk}{4\sinh 2kh} + \cos(kx - \omega t) + \frac{Hk}{8}\frac{\cosh kh\left(2\cosh^2 kh + 1\right)}{\sinh^3 kh}\cos(2kx - 2\omega t)\right] \tag{10}$$

$$\left.\begin{aligned} u &= \frac{\omega H}{2}\left[\frac{\cosh k(h+z)}{\sinh kh}\cos(kx - \omega t) + \frac{3}{8}Hk\frac{\cosh 2k(h+z)}{\sinh^4 kh}\cos(2kx - 2\omega t)\right] \\ v &= 0 \\ w &= \frac{\omega H}{2}\left[\frac{\sinh k(h+z)}{\sinh kh}\sin(kx - \omega t) + \frac{3}{8}Hk\frac{\sinh 2k(h+z)}{\sinh^4 kh}\sin(2kx - 2\omega t)\right] \end{aligned}\right\} \tag{11}$$

where H is the wave height, k is the wave number, ω is the angular frequency and h is the water depth.

2.3. CSM solver

The structural deformation of each FlexWEC is modelled using the finite element method, which is governed by the conservation of momentum.

$$\rho_s \frac{\partial^2 d_i}{\partial t^2} = \frac{\partial \sigma_{ij}}{\partial x_j} + \rho_s g_i, \tag{12}$$

where d_i is the displacement in ith direction (where $i = 1$, and 2, representing the x and z directions, respectively), ρ_s is the density of the solid, σ_{ij} is the stress tensor, and g_i is the body force due to gravity. Using the principle of virtual work, the equilibrium of the slender body in the updated Lagrangian formulation can be obtained:

$$\int_V \rho_s \ddot{d}_i \delta d_i dV + \int_V (\Delta\sigma_i + \sigma_i)\delta e_i dV + \int_V (\Delta\sigma_i + \sigma_i)\delta\eta_i dV = \int_S t_i \delta d_i dS, \tag{13}$$

where σ_i is the stress of the solid, and t_i is the surface traction, e_i and η_i are the linear and non-linear parts of the strain, δd_i, δe_i and $\delta\eta_i$ are the virtual variations of displacement and strain.

The present flexible WEC simulates under the assumption of a 2D model, resulting in a beam thickness (in the y-direction) of zero. This leads to behaviour analogous to that of a beam model. Based on the Euler-Bernoulli beam hypothesis, considering a structure with a cross-

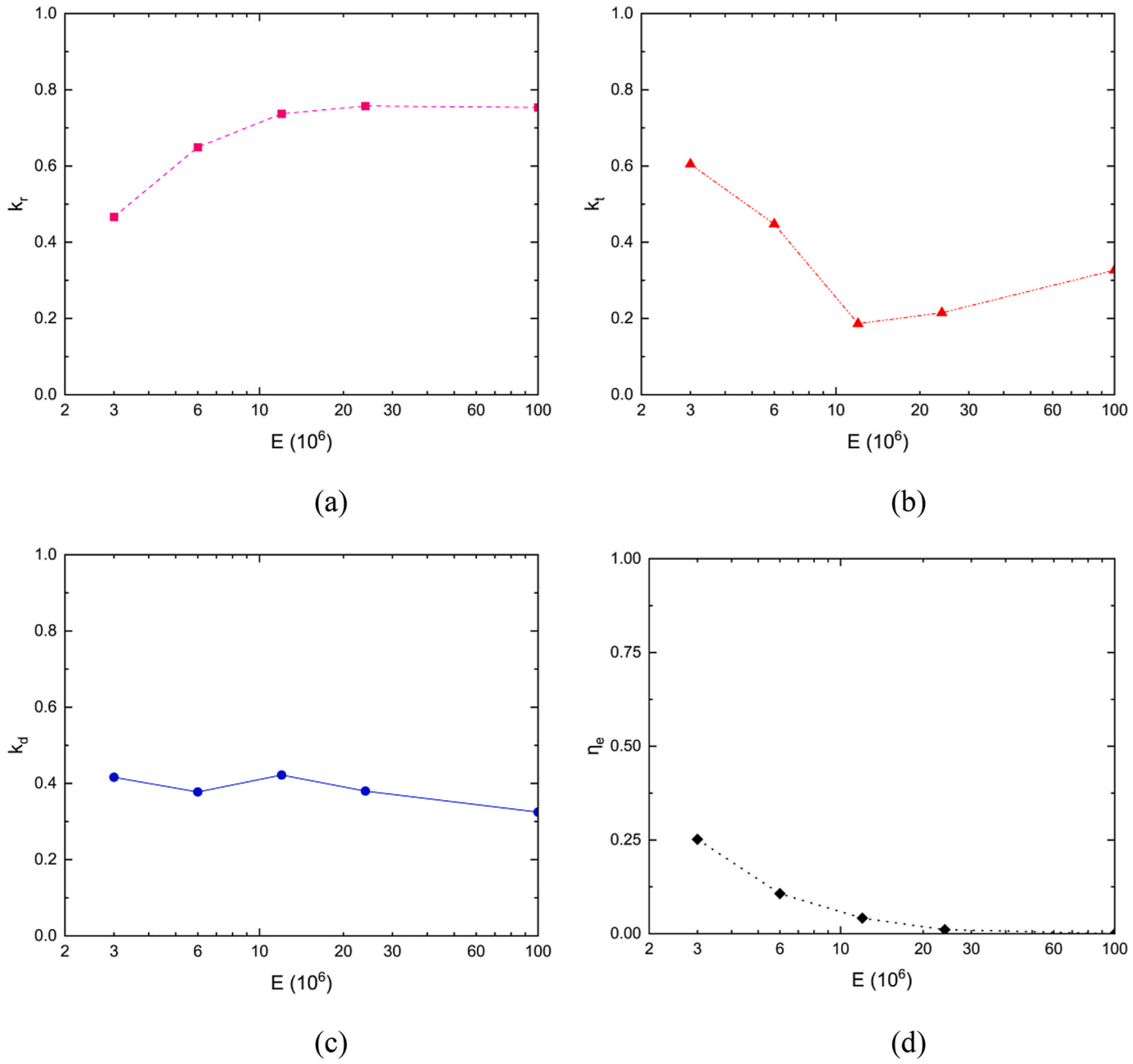

Fig. 12. Performance of the dual FlexWECs with the separating distance $\frac{d}{L} = 0.5$ under different elastic stiffness. (a) Wave reflection coefficient k_r, (b) Wave transmission coefficient k_t, (c) Wave dissipation coefficient k_d, and (d) Energy conversion efficiency η_e.

section much smaller than its longitudinal scale, each cross-section is assumed to remain rigid and orthogonal to the beam axis during the deformation process, see Fig. 3 (a). The motion of each point for the structure is obtained from the translation and rotation of the cross-section where it is located. C is the intersection of the cross-section with the central axis, then the displacement (d_1, d_2, d_3) can be obtained by the translation (δ_{1C}, δ_{2C}, δ_{3C}) and rotation (δ_{4C}, δ_{5C}, δ_{6C}), which can be written as:

$$d_1 = \delta_{1C} - y\delta_{6C} + z\delta_{5C}, d_2 = \delta_{2C} - z\delta_{4C}, \text{and } d_3 = \delta_{3C} + y\delta_{4C}. \tag{14}$$

$$\frac{\partial \delta_{2C}}{\partial x} = \delta_{6C}, \text{and } \frac{\partial \delta_{3C}}{\partial x} = -\delta_{5C}. \tag{15}$$

As shown in Fig. 3(b), the flexible slender body is discretised by several beam elements with arbitrary cross sections. Each element has two nodes situated on either side of the central axis, and each node has three translational and rotational nodal displacement increments. The middle nodes where C is located on both sides of the element between A and B are shown in Fig. 3(c). Linear polynomials are used to interpolate δ_{1C} and δ_{4C}, while cubic polynomials are used for δ_{2C} and δ_{3C}. The displacement and strain of the beam element can be obtained as follows:

$$[d] = [N][\delta^e], [e] = [B_L][\delta^e], \text{and } [\eta] = [B_N][\delta^e], \tag{16}$$

$$\boldsymbol{\delta}^e = (\delta_{1A},\ \delta_{2A},\ \delta_{3A},\ \delta_{4A},\ \delta_{5A},\ \delta_{6A},\ \delta_{1B},\ \delta_{2B},\ \delta_{3B},\ \delta_{4B},\ \delta_{5B},\ \delta_{6B}\ ), \tag{17}$$

where $[\delta^e]$ is the nodal displacement increment of one element. $[N]$ represents the shape function, $[B_L]$ and $[B_N]$ denote as the linear and nonlinear part of the strain-displacement transformation matrix. By combining Equations (16) and (13), the total nodal displacement increment of the whole structure can be defined as $[\delta]$, then the

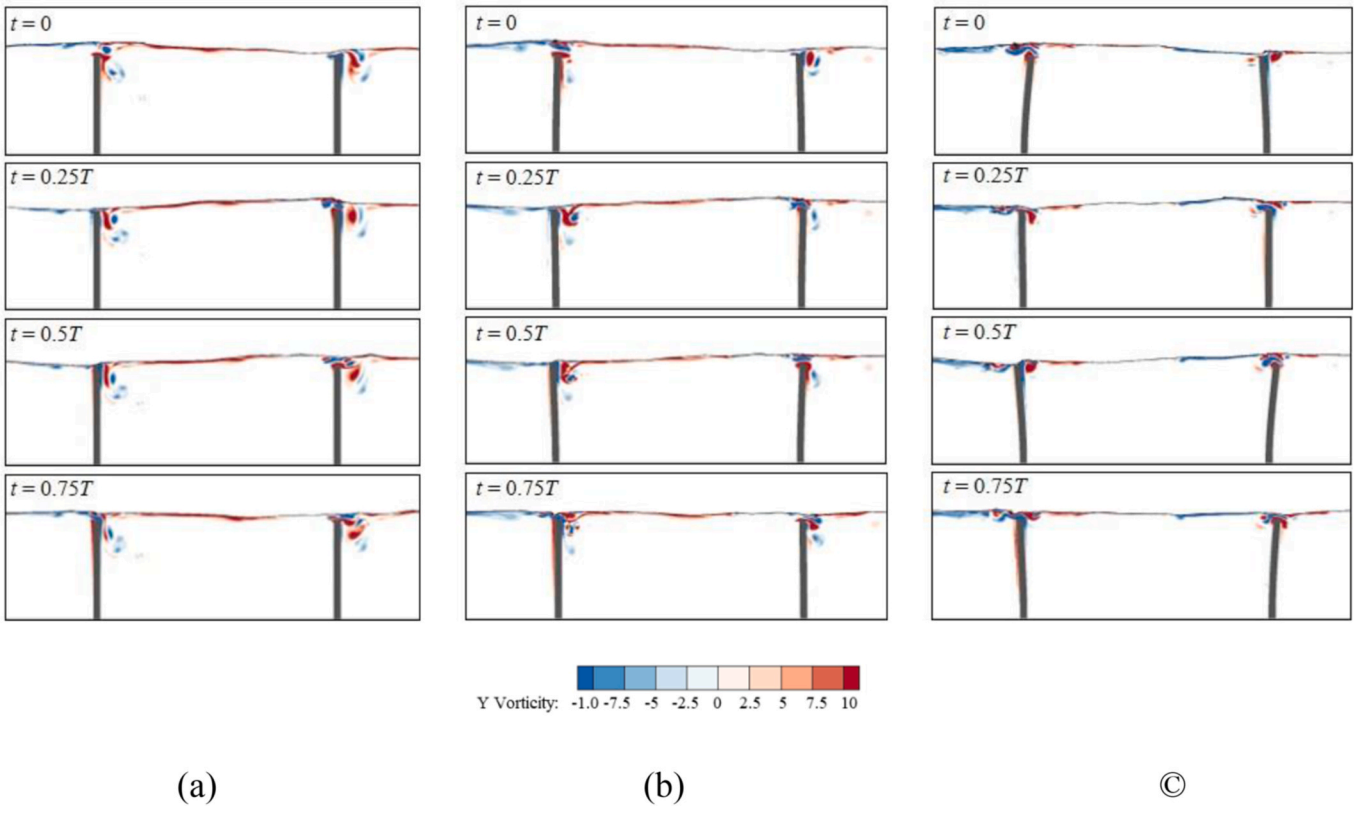

Fig. 13. Vorticity of dual FlexWECs with separation distance $d/L = \frac{1}{2}$ on various stiffness. (a) $E = 100$ MPa, (b) $E = 12$ MPa, (c) $E = 3$ MPa.

equilibrium equation of all the nodal degrees can be written as

$$[m]\{\ddot{\delta}\} + \left([k_e] + [k_g] + [\Delta k_g]\right)\{\delta\} = \{f_h\} - \{G\}, \tag{18}$$

where $\{\ddot{\delta}\}$ is the nodal acceleration, $[m]$ represents the mass matrix, $[k_e]$, $[k_g]$ and $[\Delta\ k_g]$ denote the linear stiffness matrix, geometrical stiffness matrix and high-order stiffness matrix, $\{f_h\}$ is the hydrodynamic force vector and $\{G\}$ is the body-stress vector. The simplified matrix is written as:

$$[m] = \int_{V^n} \rho_s [N]^T [N] dV, \tag{19}$$

$$[k_e] = \int_{V^n} [B_L]^T \left[\frac{\partial \sigma}{\partial \varepsilon}\right] [B_L] dV, \tag{20}$$

$$[k_g]\{\delta\} = 2\int_{V^n} [B_N]^T \{\sigma\} dV, \tag{21}$$

$$[\Delta k_g] = 2\int_{V^n} [B_N]^T \left[\frac{\partial \sigma}{\partial \varepsilon}\right] [B_L] dV, \tag{22}$$

$$\{G\} = \int_{V^n} [B_L]^T \{\sigma\} dV, \tag{23}$$

where $\partial\sigma_i/\partial\varepsilon_j$ are the material coefficients. Noting that PTO of the WEC could be modelled by further incorporating a damping term in the above equations, this is however out of the scope of the present work.

The vertical-wall structure is modelled as a cantilevered flexible beam bending on its first mode of deformation, for which the motion is described by that of a damped oscillator. Beam type of flexible WECs modelling has been discussed in Refs. [33,43], introducing the following assumptions: (a) the DEG beam is a lossless elastic material, to simply in material selection, and (b) The stretch is variable throughout the DEG beam and it is everywhere equal-biaxial.

Based on these assumptions, non-linear beam theory is applicable. The local position of the beam is a function of the maximal beam-tip deflection and is proportional to the total beam loading and the elastic restoring force. Consider a beam of length h_s, thickness b, fixed at one end (see Fig. 2). For small values of b, it is assumed that the beam primarily undergoes bending in the preferred x-direction, and any elementary section of the beam remains perpendicular to the neutral axis. With such assumptions, the Euler-Bernoulli hypothesis can apply. In the current study, the parameters of FlexWEC are $h_s = 0.28$ m, $b = 0.02$ m, and $E = 6$ MPa, with the beam element used for discretisation. Theoretical and numerical solutions predicting self-oscillating frequencies and formations under small beam deformation conditions were compared. The analytical formulae of the beam's deformation in mode shapes are given below [49].

$$f_n = \frac{1}{2\pi}\left(\frac{\sqrt{k_n}}{h_s}\right)^2 \sqrt{\frac{Eb^2}{12\rho}} \tag{24}$$

$$d_n = cosh\left(\frac{\sqrt{k_n}}{h_s}z\right) - cos\left(\frac{\sqrt{k_n}}{h_s}z\right) - \frac{cosh\left(\sqrt{k_n}\right) + cos\left(\sqrt{k_n}\right)}{sinh\left(\sqrt{k_n}\right) + sin\left(\sqrt{k_n}\right)}\left(sinh\left(\frac{\sqrt{k_n}}{h_s}z\right) - sin\left(\frac{\sqrt{k_n}}{h_s}z\right)\right) \tag{25}$$

where k_n is mode shape factor ($k_n = 3.52$ for mode 1), d_n refers to the displacement of a beam in a particular mode and z represents the spatial coordinate along the length of the beam.

The relative error in the first natural frequency $|f\text{-}f_1|/f_1$ for different numbers of beam elements is shown in Fig. 4(a) to determine the convergence number of the beam elements. When the number of

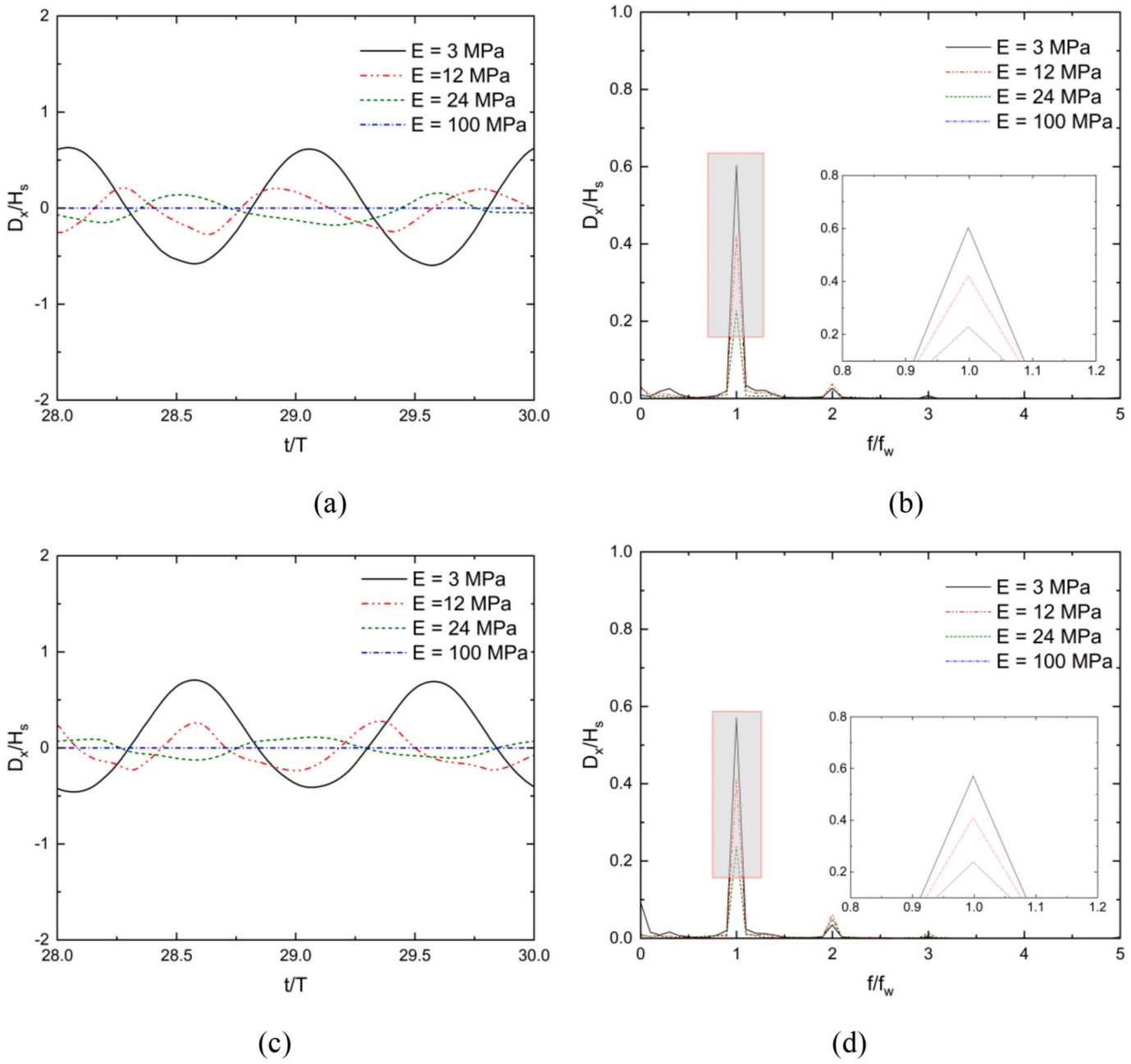

Fig. 14. Structure deformation D_x/H_s with different structure stiffness (a) Time series for body #1, (b) FFT analysis for body #1, (c) Time series for body #2, (d) FFT analysis for body #2.

elements is set to 28, the relative error is $5e^{-8}$, and Fig. 4(b) demonstrates that the corresponding natural mode matches the theoretical solution. Therefore, in the subsequent simulations, 28 beam elements are employed for the discretisation of each FlexWEC device.

2.4. FSI coupling framework

The coupling of two-phase flow with structural dynamics is achieved through the implementation of boundary conditions, encompassing no-slip, no-penetration, and traction conditions:

$$\mathbf{u} = \left\{ \frac{\partial d_1}{\partial t}, \quad \frac{\partial d_2}{\partial t}, \quad \frac{\partial d_3}{\partial t} \right\}, \tag{26}$$

$$-p\mathrm{n} + \mu\left(\nabla \mathrm{u} + \nabla \mathrm{u}^T\right) \bullet \mathrm{n} = \tau \tag{27}$$

The no-slip, no-penetration boundary conditions between the fluid domain and the solid domain are implemented using the Immersed Boundary Method (IBM). IBM leverages nonconformal boundary surfaces through a Cartesian mesh to mimic the presence of a body. This is achieved through the imposition of the momentum forces, which are included as additional terms in the momentum equation [50,51]. This ensures that the Lagrangian solid can move and deform in the fluid grids arbitrarily. This study utilises the coupling approach developed by Ref. [31], which efficiently handles the interaction between the beam model and two-phase flow.

The meshless surface reconstruction method, as described by Ref. [31], is employed to determine the occupation of the beam. In this approach, the velocity nodes located within the solid body are designated as solid nodes, while the velocity nodes within the fluid domain and immediately adjacent to the immersed boundary are referred to as

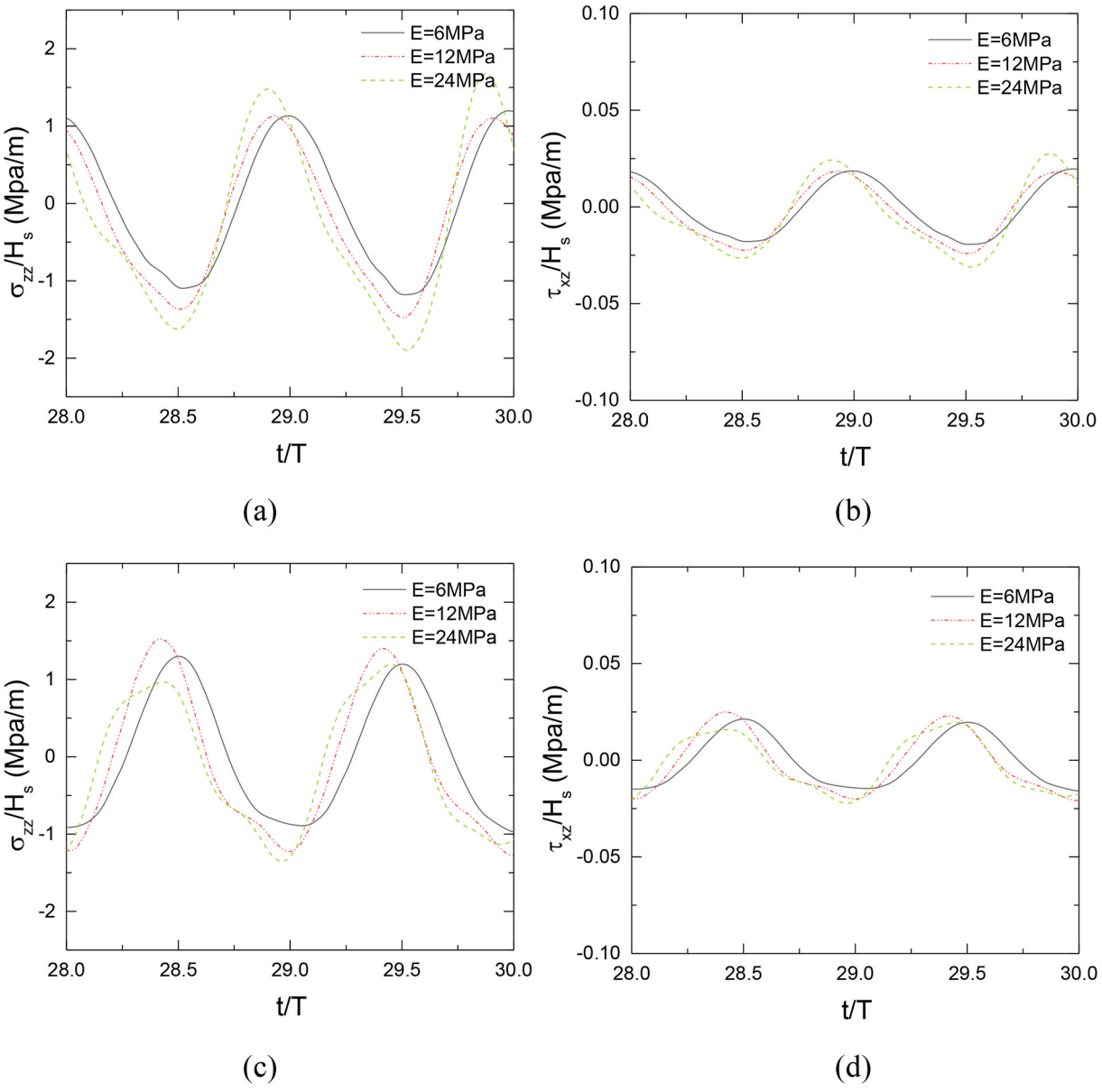

Fig. 15. Structure stress with different structure stiffness (a) Normal stress σ_{zz} for the upstream device, (b) Shear stress τ_{xz} for the upstream device, (c) Normal stress σ_{zz} for the downstream device, (d) Shear stress τ_{xz} for the downstream device.

boundary nodes. All other velocity nodes are categorized as fluid nodes. Fig. 5 illustrates the influence of the structure on the flow field, where momentum forcing is imposed at the solid nodes and boundary nodes. The momentum forces are given by:

$$\mathbf{f} = \frac{\rho^{n+1}\mathbf{U} - \rho^{n}\mathbf{u}^{n}}{\Delta t} + L_{conv}(\mathbf{u}^{n}) - L_{diff}(\mathbf{u}^{n}) + \nabla p^{n} - \rho^{n+1}\mathbf{g}, \tag{28}$$

The velocity **U** at the boundary nodes is computed using a second-order velocity reconstruction method that incorporates the immersed boundary velocity and neighbouring fluid nodes. Prior to the velocity reconstruction process, a preliminary step is executed to acquire the neighbouring fluid velocity $\mathbf{u}^{**}$ for the reconstruction stencil at time step $n+1$. This step ensures a robust and accurate velocity reconstruction process, which is essential for capturing the fluid-structure interaction dynamics in the system.

$$\rho^{n+1}\mathbf{u}^{**} = \rho^{n}\mathbf{u}^{n} + \Delta t\left[- L_{conv}(\mathbf{u}^{n}) + L_{diff}(\mathbf{u}^{n}) - \nabla p^{n} + \mathbf{f}^{n+1}\right]. \tag{29}$$

The traction condition is employed to calculate the hydrodynamic forces acting on the structure. The hydrodynamic force vector $\{f_h\}$ is determined through the integration of the pressure and the viscous stress, multiplied by the shape functions of the beam:

$$\{f_h^{n+1}\} = f_{hI}^{n+1} = \int_{S^n}\left[- pn_j + \mu\left(\frac{\partial u_i}{\partial x_j} + \frac{\partial u_j}{\partial x_i}\right)n_i\right]N_{jI}dS, \tag{30}$$

This approach allows for an accurate representation of the hydrodynamic forces exerted on the structure, taking into account the fluid-structure interaction and the surrounding flow conditions. To summarise, the complete FSI coupling procedure is shown in Fig. 6.

2.5. Parameters for data analysis

Wave transmission coefficient k_t, Wave reflection coefficient k_r are derived from the following equations:

$$k_t = \frac{H_t}{H_i} \tag{31}$$

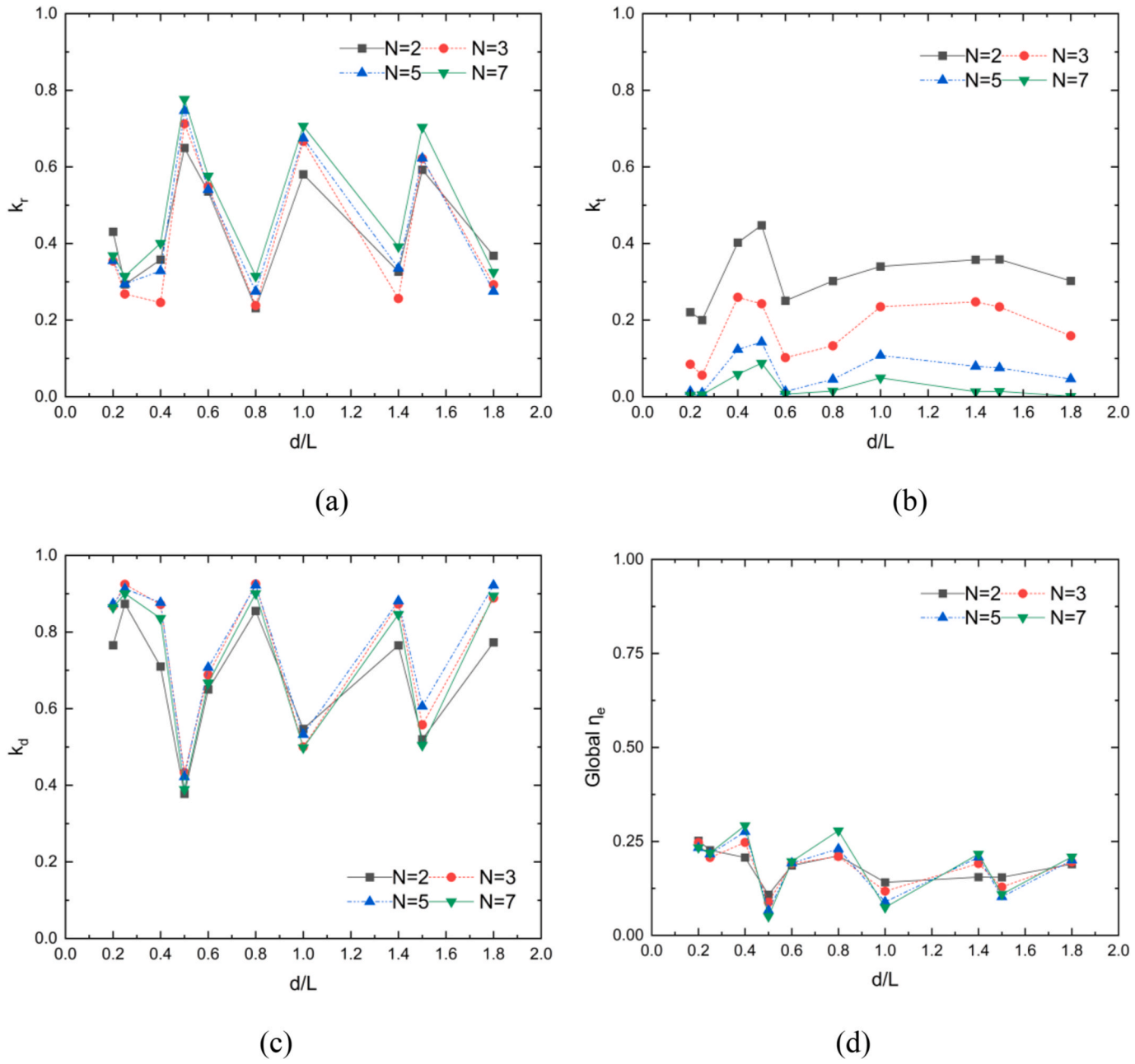

Fig. 16. Performance of FlexWEC array with various separating distance $\frac{d}{L}$ under different WEC number N. (a) Wave reflection k_r, (b) Wave transmission k_t, (c) wave dissipation k_d coefficients and (d) Energy conversion efficiency η_e.

$$k_r = \frac{H_r}{H_i} \tag{32}$$

where H_t, H_r *and* H_i indicate transmitted, reflected and incident wave height, respectively. The reflection wave height H_r is calculated by the two-point method [38].

The dissipation energy coefficient k_d is calculated as follows [52]:

$$k_d = 1 - {k_t}^2 - {k_r}^2 \tag{33}$$

The energy conversion efficiency η_e in this study is considered as the deformation energy of one FlexWEC, divided by the total incident wave energy [53]. It has the expression:

$$\eta_e = E_p / E_w \tag{34}$$

E_p is given in Equation (35), and E_w is calculated as Equation (36) [24].

$$E_p = \frac{2}{T} \sum_{m=1}^{n} \frac{1}{2} \frac{EI{\Delta\theta_m}^2}{\Delta z_m} \tag{35}$$

$$E_w = \frac{1}{16} \frac{\rho g H_i^2 \omega}{k} \left(1 + \frac{2kh}{sinh\ 2\ kh}\right) \tag{36}$$

where, I is the cross-sectional moment of inertia of a two-dimensional beam, EI represents the structural rigidity, $\Delta\theta$ is the rotation angle of each element, k and T are the incident wave number and length, h is the water depth, Δz is the beam element length, m is the element number of the FlexWEC beam and n is the element number.

3. Verification

Detailed verification for the present computational approach is

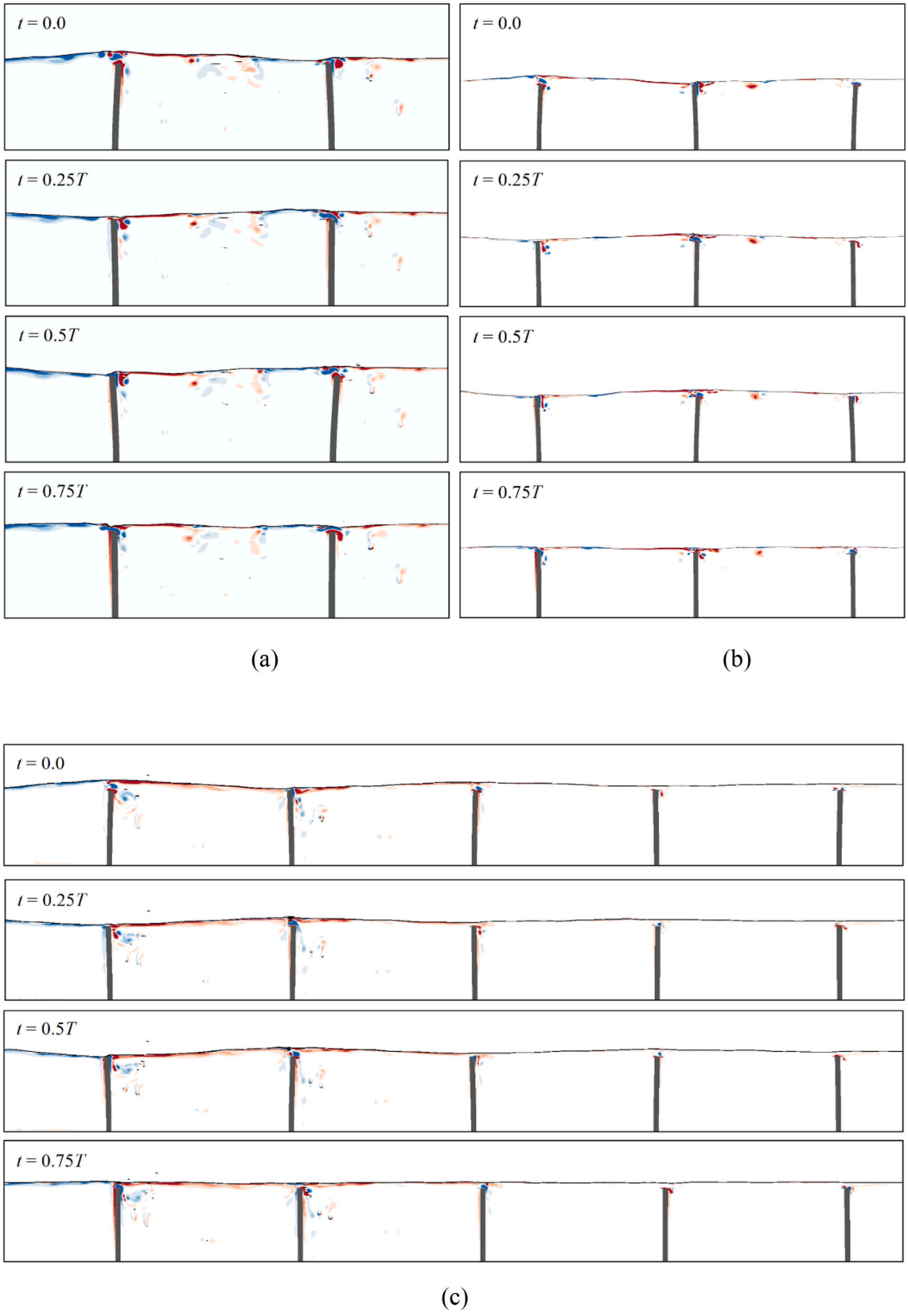

Fig. 17. Vorticity observation of cases with separation distance of $\frac{d}{L} = 0.5$ for various WEC number (a) $N = 2$, (b) $N = 3$, (c) $N = 5$, (d) $N = 7$.

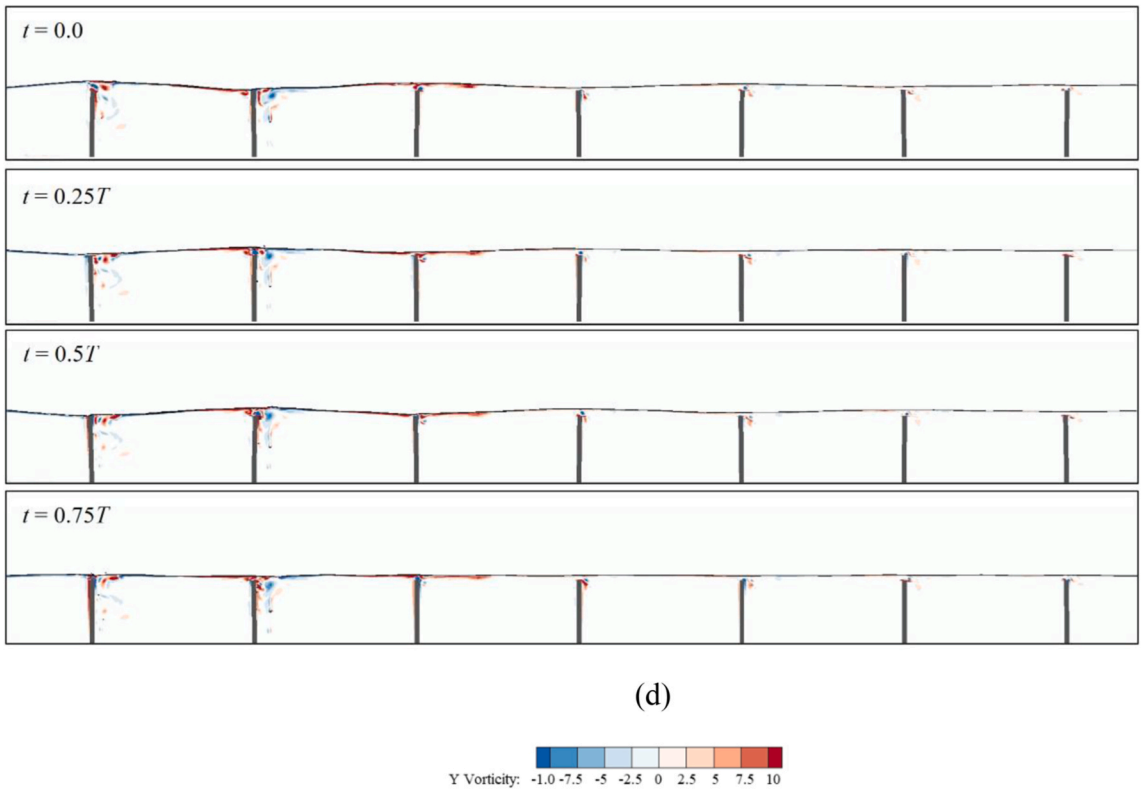

Fig. 17. (*continued*).

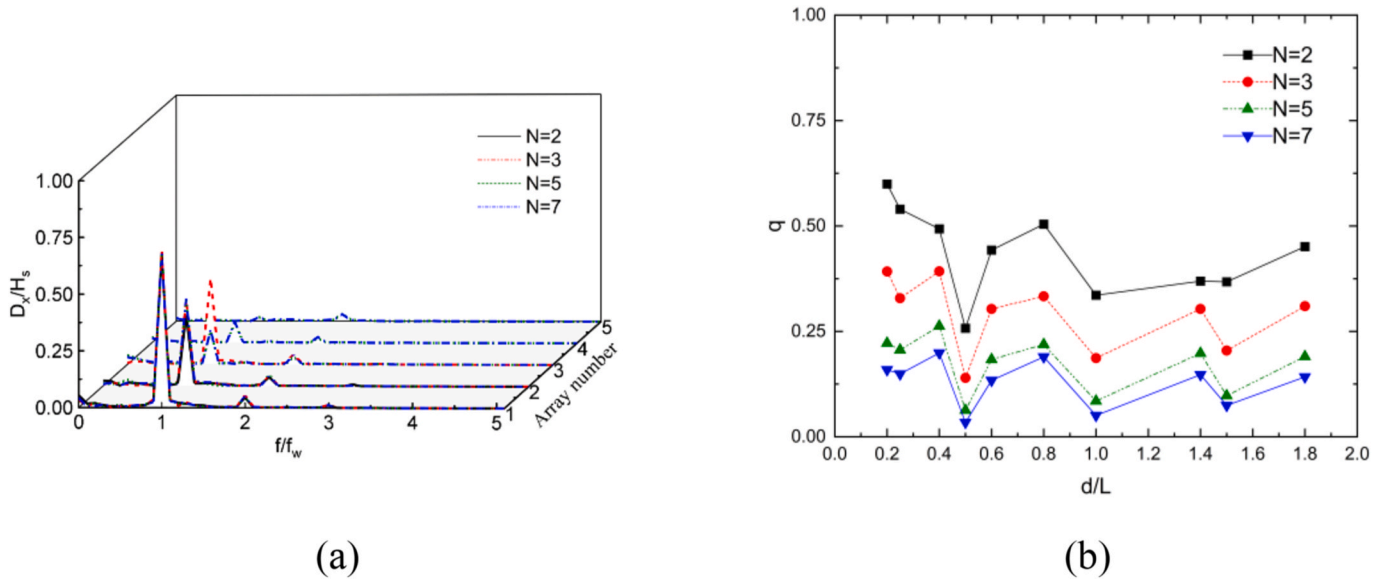

Fig. 18. (a) FFT analysis on the horizontal beam deflection $\frac{D_x}{H_s}$ (a) FFT analysis on the horizontal beam deflection $\frac{D_x}{H_s}$ and (b) The influence factor q under different WEC numbers.

conducted against Hu et al. [33], in which the authors studied the interactions between waves and a single deforming seawall. The present computational approach is used to reproduce the cases in Ref. [33], and comparison is made in terms of both structural deformation and the surrounding wave field. The corresponding sets of parameters for this verification study are summarised in Table 1, and one of the simulation cases is shown in Fig. 7.

The computational mesh and time step size were chosen based on a parameter dependence check, using the case of $\beta = 0.1$. In the far-field region, a uniform grid with $\Delta x = L/50$ and $\Delta z = H/20$ was employed to reduce wave attenuation. Within the region where the beam is expected to move, the grid was locally refined. Table 2 shows the refined computational grid spacing in three mesh densities. To ensure that at least one grid covers the thickness of the structure, $\Delta x = b/2$ is the limit of the coarsest mesh. The time histories of the response displacement of the free end of the beam in the x direction D_x based on the three different meshes are compared in Fig. 8(a). The displacements calculated from the three meshes oscillate regularly at almost the same frequency. At the

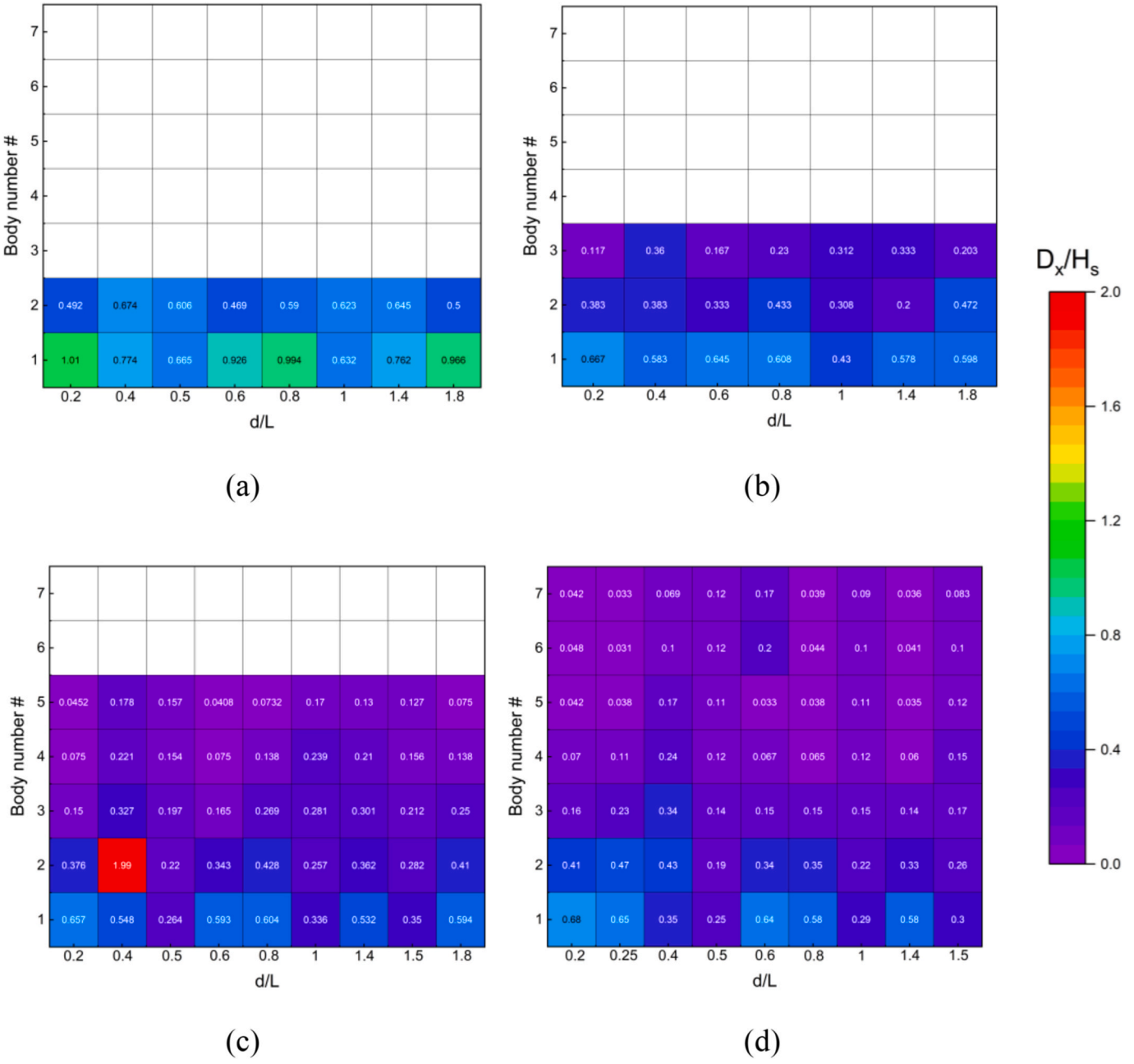

Fig. 19. Non-dimensionalised horizontal structural deformation D_x/H_s of each body with various separating distances and device numbers (a) $N = 2$, (b) $N = 3$, (c) $N = 5$ and (d) $N = 7$.

peaks and valleys, there are differences in the coarse grid compared to the remaining two grids. To make further comparisons, the wave surface elevation η/H was recorded at a location 2.315 m ahead of the beam, as shown in Fig. 8(b). The difference between the medium and the fine was relatively small, while the coarse grid showed a phase deviation.

The simulation results from different meshes are also compared quantitatively with [33] in Table 3. The relative errors of the maximum displacement in Medium and Fine grids are within 2%, so does their difference for the reflection coefficient. Based on the above analysis the Medium mesh density is selected for the following simulations in this study.

The convergence of the time step is further analysed using the Medium grid. The simulations are performed with three fixed time step $\Delta t = 1/625T$, $1/1250T$ and $1/2500T$ to ensure a Courant number $C_r \leq 0.6$, 0.3 and 0.15 during the simulation process. Table 4 summarises the relative errors of the maximum displacement of the free end and the reflection coefficient. When $\Delta t = 1/1250T$, the relative error in the maximum displacement is 2.277% and the difference in reflection coefficient from $\Delta t = 1/2500T$ is 0.892%. This informed the choice that $\Delta t = 1/1250T$ will be used in the subsequent simulations.

To further verify the present model, the maximum displacement D_x/A_{min}, reflection k_r and transmission k_t coefficient against the stiffness coefficient β are analysed and shown in Fig. 9. We achieved good agreement with the results obtained by Ref. [33]. As the stiffness of the beam increases, the displacement of the beam decreases, the reflection coefficient gradually increases and the transmission coefficient decreases. Although [33] only studied one device, upon the presented verification, it is reasonable to deem that the current model is still verified when the model is extended to contain multiple devices. The incorporation of extra geometry in CFD simulations effectively manages

wave diffraction and radiation effects at the free surface due to structural motions. To ensure bounded fluid flow in multi-phase modelling, strict adherence to a Courant number below 0.5 is maintained throughout subsequent simulations, coupled with achieving a residual level of $1e^{-6}$ for robust convergence in the CFD domain. The simulations of wave interacting with multiple deforming devices are demonstrated and discussed in the next section.

4. Results and discussion

Systematic simulations are conducted to investigate the influences of (a) the number of devices N, (b) Young modulus of the device, E, and (c) the separating distance d between two devices, on the hydroelastic interaction and energy performance. The parameters used in this section is listed in Table 5.

4.1. Dual FlexWECs

The investigation starts with two FlexWECs placed in the wave domain with a separation distance $d/L = \frac{1}{2}$, as shown in Fig. 10. The wave domain extends along the x-z direction, and the selected domain height is set at 2 h to maintain consistency with the methodology outlined in Ref. [33]. To accurately capture near-wall and free surface flow, mesh refinements are strategically implemented. Four different elastic modulus values, ranging from 3 MPa to 100 MPa, are applied to both beams simultaneously.

In the prioritisation of dual-beam analysis, it is valuable to perform modal analysis to assess the vibration characteristics based on selected beam properties. The investigation into the beam's vibration characteristics was carried out independently. A single beam was placed in water with an initial deflection, and it was allowed to free decay to its neutral position. The domain sizes and beam physical properties are maintained as in the dual-beam simulation, while the second beam is removed here. The initial displacement is applied according to the first order vibration shape, which can be viewed in Fig. 11. This free-decay simulation allows for the extraction of wet mode eigenvalues of the beam. Fig. 11 illustrates the free vibration over time along with corresponding frequency response curves. The prominent peak in the frequency component indicates a potential resonance frequency for the beam.

It is important to note the natural frequencies of the beam in air and in water are different. Equations (24) and (25) give the result in air, with an example prediction of $f_1 = 2.92$ Hz when E = 6 Mpa. This is larger than the first natural frequency shown in Figs. 11(b), 1.58 Hz. The lower natural frequency of a beam in water than air is due to the added mass effect introduced by the surrounding fluids.

The reflected k_r and transmitted wave k_t coefficient against Young's modulus E for the dual beam application are shown in Fig. 12(a) and (b). Flexible cases exhibit smaller wave reflections than the rigid case, as beams with a smaller elasticity undergo a larger deformation, which in turn allows for more waves to transmit through beam oscillations. However, a turning point in k_t can be observed when $E = 12$MPa. Under this condition, k_t increases with E, which ssuggests that there exists a value of E that will lead to the smallest k_t due to the hydroelastic interaction, not always the largest E. This phenomenon was also demonstrated by Huang and Li [26]. Fig. 12(c) displays the wave dissipation k_d calculated using Equation (33). The average k_d remains close to 40%, which is the sum of energy that goes into structural deformations and fluid viscosity. The global energy conversion efficiency η_e is calculated by summing up the energy of each beam divided by the incident wave energy, as shown in Fig. 12(d). The value of η_e is predicted around 1.15% for the case of 3 MPa and decreases values of up to 25% for 24 MPa, thus demonstrating the choice of material dominates the energy performance. It is interesting to see that increasing η_e does not necessarily increase k_d. Therefore, energy that is not harnessed through deformations will still dissipate as fluid viscosity within the interaction of waves with a more rigid beam. This phenomenon can be further observed in Fig. 13, where more rigid cases show more fluid vorticity.

Fig. 13 shows the vorticity contours of the wave field around the dual FlexWECs with different stiffnesses for $T = 1.0$ s. For all the case, when $t = 0$ the wave crest reaches the former WEC and the trough reach the latter one, and it is reversed at $t = 0.5T$. However, the comparison reveals a significant difference in vortex shedding between the rigid and flexible cases. For the rigid case (see Fig. 13(a)), a part of the fluid flows into the gap of the former WEC in the form of a jet at $t = 0$, resulting in positive vortex shedding at the trailing edge of the former WEC and propagating downstream along with the negative vortex shed in the previous wave period. When $t = 0.5T$, negative vortex shedding at the trailing edge of the former WEC. For the case of $E = 3$MPa (see Fig. 13 (c)), the vortices are mainly generated by the swing of the free end of the WECs. The former WEC shed negative vortices on the trailing edge at $t = 0$ and positive vortices on the leading edge at $t = 0.5$ T. The case of $E = 12$MPa (see Fig. 13(b)) is in a transition state between the rigid WEC and flexible WEC, and the vortex field has some of the characteristics of the first two. In all the cases, the latter WEC has a similar vortex shedding process as the former one, but with a phase difference of half a wave period, which is in line of the setup that $d/L = \frac{1}{2}$.

Fig. 14 illustrates the time history and frequency responses of dimensionless deformation of the structural tip D_x/H_s with different structural stiffness. Time domain results (Fig. 14(a) and (c)) show the two beams with similar deformations. It is observed that the second beam's deformation is just slightly smaller than that of the front beam, with a reduction of less than 8% D_x/H_s throughout all structural stiffness. Frequency analysis of the beam deformation signals presented in Fig. 14(b) and (d) was conducted using the Fast Fourier Transform (FFT). The main frequency amplitude, which is consistent with the incident wave frequency, is greatly affected by the structural stiffness as it decreases with increasing stiffness. The sub-frequencies amplitudes are negligible by comparison with the main frequency.

In Fig. 15, stress results for dual beams with varying material stiffness are depicted, encompassing both normal and shear stress components. Notably, lower stress levels are observed when E = 6 MPa. This suggests a reduced likelihood of the structure experiencing peak loads, minimizing the risk of failure. Consequently, the optimal beam stiffness identified at E = 6 MPa is applied consistently throughout all subsequent simulations.

4.2. FlexWEC array of different array arrangement

Based on the insights obtained from the previous section with dual FlexWECs, this section extends the case to more devices $N = 2 - 7$, and for varying separation distances $d/L = 0.2 - 1.8$. The incident wave condition $T = 1$ s, $H_s = 0.03$ m, and E = 6 MPa are applied through all simulations in this section.

The variations of the wave reflection coefficient k_r, transmission coefficient k_t, dissipation coefficient k_d and energy conversion efficiency η_e are evaluated with various separation distances ranging $\frac{d}{L} = 0.2$ to 1.8 verse row number N, as shown in Fig. 16. (c). The resulting curves show undulating trends It can be seen from Fig. 16(d) that regardless of the number of devices deployed, the magnitude of η_e is minimal when the separation distance $\frac{d}{L}$ is equal to n × 1/2 L. This phenomenon agrees with the Bragg resonance commonly observed in wave interactions with arrays [43]. Bragg resonance can result in waves focussed in the gap between two devices, significantly reducing the energy that can be absorbed by the devices.

As shown in Fig. 16(a), wave reflection k_r is also linked with Bragg resonance. It can be seen that small k_r are noticed at the relative separation distance $\frac{d}{L} = 0.25 - 0.35$ and every two Bragg resonance frequencies, such as $d/L = 0.8$ or 1.3. Fig. 16(b) shows that k_t does not have a trend of Bragg resonance, while k_t decreases with the increasing device

number N, indicating that the wave attenuates whilst passing through each device. The transmitted wave becomes minimal when $N \geq 5$, which is particularly interesting when WECs also serve for coastal engineering purposes. From Fig. 16(c) and (d), it appears that the number of devices does not have a significant impact on the overall energy dissipation and harnessing.

Fig. 17 shows the vorticity contours of the wave field around different FlexWECs deployments at various time instants during a wave period ($t = 0, 0, 25T, 0.5T$ and $0.75T$). In Fig. 17(a) and (b), it is illustrated that strong vortexes are generated at two regions: the top of each beam, and the internal region between the two beams. Consequently, these eddies dissipate a part of wave energy. When $N \geq 5$, the vortex generation regions mainly focus on the front beams, and the magnitudes reduce within the array, (see Fig. 17(c) and (d)), the effects of the vortex are not dominated. This explains the underlying reason for deploying more devices not inducing higher k_d.

Fig. 18(a) displays the FFT analysis of horizontal beam deflection D_x/H_s with various under different WEC numbers, showing deformation results of the first five devices (Array number #1-#5). It can be seen that the three upstream WECs (#1, #2 and #3) show peaks at the main frequency, and the magnitude reduces when more devices are deployed. For results of device #5, it can be seen that its deformation is rather small as the wave has become minimal after passing through the upstream devices. This explains the underlying reason for deploying more devices not inducing higher η_e. Fig. 18(b) further assesses the influence factor (q) of four different array configurations (N = 2, 3, 5, 7) across a range of gap clearances (d/L = 0.2–1.8). This figure illustrates that array deployment predominantly induces destructive effects, with an escalation of these effects observed at Bragg resonance frequencies.

Finally, to provide an overall view and obtain an optimal condition, the deformation amplitude of each device tip D_x at all cases is plotted in Fig. 19. Accordingly to the colour contour, it can be observed that separation distance becomes more influential with increasing N. Regardless d/L, the D_x of device #1 is approximately H_s, expect Bragg resonance conditions. The maximum $\frac{D_x}{H_s}$ are observed in Fig. 19(c), reaching a value close to 2 at device #2 for $d/L = 0.35$, and $N = 5$. At this separation distance, the rest bodies within the array also experience relatively large deformations compared to the other distance. Overall, the largest structure deflection occurs in the separation region within a range of $0.28 < d/L < 0.41$. This is also deemed as the region to obtain the most energy as the large deformations, the more wave energy is converted.

5. Conclusions

This paper reported hydroelastic analysis on the interaction between an array of FlexWECs and regular waves, and investigated the overall energy performance. A fully nonlinear FSI framework is implemented based on CFD and CSM. Verification studies were conducted against a previous publication [33] to justify the accuracy of the present approach.

Based on the verified model, this paper presented a series of simulations to analyse the performance of an array of up to seven seawall-type FlexWECs. These interactions are complex and depend on many parameters related to the characteristics of both the fluid and the solid, while the present work focussed on the array arrangement specific to the number of devices and the distance between each device. It was found that Bragg resonance, similar to many previous wave interactions with multiple structures, is also evident in the present case. It occurs when the distance between devices is an integer multiple of half the incident wavelength. It is important to avoid this phenomenon in FlexWECs array deployment, as the overall energy performance becomes minimal in this case. The best energy performance of the present case was found when the separation distance is a range of 0.28–0.41 incident wavelength, and it is recommended to apply this seawall-type FlexWECs with a device number of 3 because further increasing the device number will not lead to higher energy output. Apart from renewable energy, the present application also shows excellent performance in coastal engineering, as the wave transmission with 5 devices deployed can be close to zero.

Although it is the first time that dynamic FSI simulations of multiple flexible bodies in waves are performed, the current simulation is performed in 2D. The 2D model potentially excludes wave scattering near the geometry, which could be significant for WEC arrays [54,55]. It is therefore suggested for future work to extend the model to 3D. In addition, PTO should be incorporated in future work to analyse the optimal performance of the WECs in different wave conditions, which can be modelled by adding a damping term in the deformation equations.

Data availability

All data underlying the results are available as part of the article and no additional source data are required.

CRediT authorship contribution statement

Yujia Wei: Conceptualization, Formal analysis, Methodology, Visualization, Writing – original draft, Writing – review & editing. **Chao Wang:** Data curation, Methodology, Software, Validation, Visualization, Writing – original draft, Writing – review & editing. **Wenchuang Chen:** Funding acquisition, Investigation, Methodology, Resources, Supervision, Writing – original draft, Writing – review & editing. **Luofeng Huang:** Conceptualization, Funding acquisition, Investigation, Methodology, Project administration, Resources, Supervision, Visualization, Writing – original draft, Writing – review & editing.

Declaration of competing interest

The authors declare that they have no known competing financial interests or personal relationships that could have appeared to influence the work reported in this paper.

Acknowledgements

L.H. acknowledges grants from Innovate UK (No. 10048187, 10079774, 10081314) and the Royal Society (IEC\NSFC\223253, RG \R2\232462). W.C. acknowledges the National Natural Science Foundation of China (Grant No. 52201349, 52311530078), Guangdong Basic and Applied Basic Research Foundation (Grant No. 2023A1515012224), Open Research Fund Program of State Key Laboratory of Hydroscience and Engineering (Grant No. sklhse-2022-B-05).

References

[1] A. Clément, P. McCullen, A. Falcão, A. Fiorentino, F. Gardner, K. Hammarlund, G. Lemonis, T. Lewis, K. Nielsen, S. Petroncini, Wave energy in Europe: current status and perspectives, Renew. Sustain. Energy Rev. 6 (5) (2002) 405–431.
[2] J. Falnes, A review of wave-energy extraction, Mar. Struct. 20 (4) (2007) 185–201.
[3] B. Guo, T. Wang, S. Jin, S. Duan, K. Yang, Y. Zhao, A review of point absorber wave energy converters, J. Mar. Sci. Eng. 10 (10) (2022).
[4] A. Babarit, Ocean Wave Energy Conversion: Resource, Technologies and Performance, Elsevier, 2017.
[5] A. Babarit, J. Hals, M.J. Muliawan, A. Kurniawan, T. Moan, J. Krokstad, Numerical benchmarking study of a selection of wave energy converters, Renew. Energy 41 (2012) 44–63.
[6] E. Renzi, S. Michele, S. Zheng, S. Jin, D. Greaves, Niche applications and flexible devices for wave energy conversion: a review, Energies 14 (20) (2021) 6537.
[7] I. Collins, M. Hossain, W. Dettmer, I. Masters, Flexible membrane structures for wave energy harvesting: a review of the developments, materials and computational modelling approaches, Renew. Sustain. Energy Rev. (2021) 151.
[8] B. Ali, K. Fatima, Mahnoor, Mathematical model validation of floating PV parks impact on the growth of green algae using experimental chamber, Energy Sources, Part A Recovery, Util. Environ. Eff. 45 (1) (2023) 804–816.
[9] Y. Wei, J. Barradas-Berglind, M. Van Rooij, W. Prins, B. Jayawardhana, A. Vakis, Investigating the adaptability of the multi-pump multi-piston power take-off system for a novel wave energy converter, Renew. Energy 111 (2017) 598–610.

[10] D.-z. Ning, D. Mu, R.-q. Wang, R. Mayon, Experimental and numerical investigations on the solitary wave actions on a land-fixed OWC wave energy converter, Energy 282 (2023) 128363.
[11] B. Zhou, Y. Wang, Z. Zheng, P. Jin, D. Ning, Power generation and wave attenuation of a hybrid system involving a heaving cylindrical wave energy converter in front of a parabolic breakwater, Energy 282 (2023) 128364.
[12] Z.Y. Tay, Performance and wave impact of an integrated multi-raft wave energy converter with floating breakwater for tropical climate, Ocean Eng. 218 (2020) 108136.
[13] Z.Y. Tay, Y. Wei, Power enhancement of pontoon-type wave energy convertor via hydroelastic response and variable power take-off system, J. Ocean Eng. Sci. 5 (1) (2020) 1–18.
[14] V. Heller, 8.04 - Development of wave devices from initial conception to commercial demonstration, Comprehen. Renew. Energy 8 (2012) 79–110, https://doi.org/10.1016/B978-0-08-087872-0.00804-0.
[15] G. Moretti, M. Santos Herran, D. Forehand, M. Alves, H. Jeffrey, R. Vertechy, M. Fontana, Advances in the development of dielectric elastomer generators for wave energy conversion, Renew. Sustain. Energy Rev. 117 (2020).
[16] Y. Bar-Cohen, P. Jean, A. Wattez, G. Ardoise, C. Melis, R. Van Kessel, A. Fourmon, E. Barrabino, J. Heemskerk, J.P. Queau, Standing Wave Tube Electro Active Polymer Wave Energy Converter, in Electroactive Polymer Actuators and Devices (EAPAD) 2012, 2012.
[17] R. Pelrine, R.D. Kornbluh, J. Eckerle, P. Jeuck, S. Oh, Q. Pei, S. Stanford, Dielectric elastomers: generator mode fundamentals and applications, Smart Structures and Materials 2001: Electroactive Polymer Actuators and Devices 4329 (2001) 148–156.
[18] Edinburgh, T.u.o, PolyWEC: New Mechanisms and Concepts for Exploiting Electroactive Polymers for Wave Energy Conversion, 2022 [cited 2023 19/07].
[19] Edinburgh, T.u.o. ELASTO Project, the University of Edinburgh School of Engineering Policy and Innocation Group. [cited 2023 19/07].
[20] CORDIS, European Commision CORDIS EU Research Results, New Mechanisms and Concepts for Exploiting Electroactive Polymers for Wave Energy Conversion, 2020 [cited 2023 19/07].
[21] WES-PTO. Project from Wave Energy Scotland, Novel Wave Energy Converter. [cited 2023 19/07].
[22] NREL, How Wave Energy Could Go Big by Getting Smaller, 2021 [cited 2023 30/07].
[23] F.J.M. Farley, R.C.T. Rainey, Distensible tube wave energy converter. US Patent 7,980,071 (2011).
[24] Q.P. Cao, M.O. Esangbedo, S.J. Bai, C.O. Esangbedo, Grey SWARA-FUCOM weighting method for contractor selection MCDM problem: a case study of floating solar panel energy system installation, Energies 12 (13) (2019).
[25] Wave_Energy_Scotland, Direct Generation WEC Concept Creation Competition. Technical Report, 2023.
[26] D.F.K. Benra, J. H, J. Pei, S. Schuster, B. Wan, A comparison of one-way and two-way coupling methods for numerical analysis of fluid-structure interactions, J. Appl. Math. 2011 (2011) 1–16.
[27] A. Babarit, J. Singh, C. Mélis, A. Wattez, P. Jean, A linear numerical model for analysing the hydroelastic response of a flexible electroactive wave energy converter, J. Fluid Struct. 74 (2017) 356–384.
[28] S. Zheng, S. Michele, H. Liang, M.H. Meylan, D. Greaves, Wave power extraction from a floating elastic disk-shaped wave energy converter, J. Fluid Mech. 948 (2022).
[29] J.C. Selby, M.A. Shannon, Inflation of a circular elastomeric membrane into a horizontally semi-infinite liquid reservoir of finite vertical depth: quasi-static deformation model, Int. J. Eng. Sci. 47 (5–6) (2009) 700–717.
[30] A. Eriksson, A. Nordmark, A. Patil, Y. Zhou, Parametric stability investigations for hydro-statically loaded membranes, Comput. Struct. 174 (2016) 33–41.
[31] C. Wang, B. Ren, P. Lin, A coupled flow and beam model for fluid–slender body interaction, J. Fluid Struct. (2022) 115.
[32] X. Li, Q. Xiao, A numerical study on an oscillating water column wave energy converter with hyper-elastic material, Energies 15 (22) (2022) 8345.
[33] Z. Hu, L. Huang, Y. Li, Fully-coupled hydroelastic modeling of a deformable wall in waves, Coast Eng. 179 (2023).
[34] L. Huang, Y. Li, Design of the submerged horizontal plate breakwater using a fully coupled hydroelastic approach, Comput. Aided Civ. Infrastruct. Eng. 37 (7) (2022) 915–932.
[35] L. Huang, K. Ren, M. Li, Ž. Tuković, P. Cardiff, G. Thomas, Fluid-structure interaction of a large ice sheet in waves, Ocean Eng. 182 (2019) 102–111.
[36] T. Attili, V. Heller, S. Triantafyllou, Wave impact on rigid and flexible plates, Coast Eng. 182 (2023) 104302.
[37] L. Huang, Y. Li, D. Benites-Munoz, C.W. Windt, A. Feichtner, S. Tavakoli, J. Davidson, R. Paredes, T. Quintuna, E. Ransley, A review on the modelling of wave-structure interactions based on OpenFOAM, OpenFOAM® Journal 2 (2022) 116–142.
[38] S. Zheng, M.H. Meylan, G. Zhu, D. Greaves, G. Iglesias, Hydroelastic interaction between water waves and an array of circular floating porous elastic plates, J. Fluid Mech. 900 (2020).
[39] Y. Li, C.C. Mei, Multiple resonant scattering of water waves by a two-dimensional array of vertical cylinders: linear aspects, Phys. Rev. 76 (1) (2007) 016302.
[40] E. Renzi, F. Dias, Relations for a periodic array of flap-type wave energy converters, Appl. Ocean Res. 39 (2013) 31–39.
[41] D. Zhang, Z.-M. Yuan, J. Du, H. Li, Hydrodynamic modelling of large arrays of modularized floating structures with independent oscillations, Appl. Ocean Res. 129 (2022).
[42] A. Babarit, On the park effect in arrays of oscillating wave energy converters, Renew. Energy 58 (2013) 68–78.
[43] C. Nové-Josserand, R. Godoy-Diana, B. Thiria, Interference model for an array of wave-energy-absorbing flexible structures, Phys. Rev. Appl. 11 (3) (2019).
[44] D. Khojasteh, A. Shamsipour, L. Huang, S. Tavakoli, M. Haghani, F. Flocard, M. Farzadkhoo, G. Iglesias, M. Hemer, M. Lewis, A large-scale review of wave and tidal energy research over the last 20 years, Ocean Eng. 282 (2023) 114995.
[45] C. Wang, H. Xu, Y. Zhang, W. Chen, Hydrodynamic investigation on a three-unit oscillating water column array system deployed under different coastal scenarios, Coast Eng. (2023) 104345.
[46] Y. Goda, Y. Suzuki, Estimation of incident and reflected waves in random wave experiments, Coast Eng. 1976 (1976) 828–845.
[47] H. Choi, P. Moin, Effects of the computational time step on numerical solutions of turbulent flow, J. Comput. Phys. 113 (1) (1994) 1–4.
[48] B.P. Leonard, A stable and accurate convective modelling procedure based on quadratic upstream interpolation, Comput. Methods Appl. Mech. Eng. 19 (1) (1979) 59–98.
[49] V. Giurgiutiu, Structural Health Monitoring: with Piezoelectric Wafer Active Sensors, Elsevier, 2007.
[50] C. Liu, C. Hu, An efficient immersed boundary treatment for complex moving object, J. Comput. Phys. 274 (2014) 654–680.
[51] W. Kim, H. Choi, Immersed boundary methods for fluid-structure interaction: a review, Int. J. Heat Fluid Flow 75 (2019) 301–309.
[52] D. Ning, X. Zhao, M. Göteman, H. Kang, Hydrodynamic performance of a pile-restrained WEC-type floating breakwater: an experimental study, Renew. Energy 95 (2016) 531–541.
[53] L. Huang, Z. Hu, Y. Li, G. Thomas, Fully-coupled CFD+ CSM Analysis on an Elastic Floating/Submerged Plate for Wave Energy Harvest, *IN MARINE TECHNOLOGY, Rome, Italy*, 2022.
[54] D. Benites-Munoz, L. Huang, G. Thomas, Optimal array arrangement of oscillating wave surge converters: an analysis based on three devices, Renew. Energy 222 (2024) 119825.
[55] W. Chen, Z. Huang, Y. Zhang, L. Wang, L. Huang, Hydrodynamic performance of a three-unit heave wave energy converter array under different arrangement, Renew. Energy 221 (2024) 119808.